STARGATE : a new instrument for high-resolution photodissociation spectroscopy of cold ionic species

Raghed Bejjani,[1, a)] Anthony Roucou,[1, a)] Xavier Urbain,[1] Konstantin Moshkunov,[1] Guilhem Vanlancker,[1] and Clément Lauzin[1]

Institute of Condensed Matter and Nanosciences, Université catholique de Louvain, B-1348 Louvain-la-Neuve, Belgium

(Dated: 21 January 2021)

STARGATE (Spectroscopy of Transient Anions and Radicals by Gated and Accelerated Time-of-flight Experiment) is a new spectrometer developed in UCLouvain. This instrument measures high-resolution photodissociation spectra of mass-selected ions by the combination of a Time-Of-Flight (TOF) spectrometer including a specific gating, bunching and re-referencing unit with a nanosecond pulsed dye laser, a pulsed deflection and an energy selector. The ionic species are generated in a supersonic jet expansion by means of an electric discharge or by the impact of electrons coming from an electron gun. The versatility of the molecular systems which can be addressed by this instrument is illustrated by the presentation of mass spectra of cations, anions and ionic clusters formed from different gas mixtures and backing pressures. The high-resolution spectrum of the $\widetilde{A}^2\Sigma^+(002) \leftarrow \widetilde{X}^2\Pi_{3/2}(000)$ and $\widetilde{A}^2\Sigma^+(002) \leftarrow \widetilde{X}^2\Pi_{1/2}(000)$ rovibronic bands of N_2O^+ has been measured and analysed to provide refined molecular parameters in the $\widetilde{A}^2\Sigma^+(002)$ upper state. The $\widetilde{A}^2\Sigma^+(002) \leftarrow \widetilde{X}^2\Pi_{3/2}(000)$ band has been used to evaluate the quality of the experimental set-up in terms of rotational temperature, time of measurement for certain signal to noise ratio and the accuracy of the determination of the wavenumber scale.

I. INTRODUCTION

Action spectroscopy has witnessed a tremendous development in several scientific directions since the first studies in atomic and molecular physics[1,2]. This interest comes from the attractive combination of the sensitivity of mass spectrometry and the tunability of laser radiation. After these pioneering works, ionic cluster spectroscopy has started with the works of Schwarz[3] and the important contribution of Y. T. Lee[4–6]. This track has been followed and expanded by many others with improvements for every part of a typical action spectrometer, i.e. the ion source, the mass spectrometer and the light source. A variety of mass spectrometers have been used like time of flight-mass spectrometers (TOF-MS)[7] and Fourier-transform ion cyclotron resonance mass spectrometers (FT-ICR-MS)[8]. Supersonic expansion has been associated with different ionization means including electronic impact[3], electric discharge[9] and laser vaporization[10,11]. The electrospray was then used for mass spectrometry of large biomolecules[12] and infrared photodissociation spectroscopy[13]. Several continuous and pulsed light sources were used with these techniques using lasers[4], free-electron lasers[8] and synchrotron radiation[7]. Variations on the measured quantity were reported including the counting of electrons[14], fragmentation products[15], products of light induced bimolecular reactions[16] or recently the determination of the magnitude of the inhibition of complex formation[17]. This last example has led to the measurement of the high-resolution spectra of numerous molecular cations including C_{60}^+ [18] and CH_5^+[19] in the infrared. A review of photodissociation studies with these techniques in the infrared, visible and ultraviolet spectral ranges was carried out by Bieske and Dopfer[15] covering the years from 1986 to 2000. In parallel the measurement of photo-electronic spectra of neutral molecules[20] and anions[14], has been the subject of important developments to retrieve information on the ionization threshold[21], the cation structure[22] and transition states in chemical reaction[23]. Finally such techniques were also applied to study biological molecules such as peptides or glucans[24–26].

In this study we report on the building of the STARGATE photo-fragmentation spectrometer which aims at measuring spectral properties of positively or negatively charged molecules and/or of ionic complexes. We detail the different parts of the STARGATE instrument including the ion source and the TOF-MS in section II and the photodissociation setup in section III. The application to high resolution photodissociation spectroscopy is discussed in section IV. This section focuses first on the global analysis of the rotationally resolved $\widetilde{A}^2\Sigma^+(002) \leftarrow \widetilde{X}^2\Pi_{3/2}(000)$ and $\widetilde{A}^2\Sigma^+(002) \leftarrow \widetilde{X}^2\Pi_{1/2}(000)$ rovibronic bands of N_2O^+, where the vibrational quantum numbers v_1,v_2,v_3 are indicated in parentheses, i.e. $(v_1v_2v_3)$. This analysis provides improved molecular constants for the $\widetilde{A}^2\Sigma^+(002)$ upper state. These improved parameters are then used to evaluate the rotational temperature of the cations in different experimental conditions. Repeated measurements of the $\widetilde{A}^2\Sigma^+(002) \leftarrow \widetilde{X}^2\Pi_{3/2}(000)$ allow us to evaluate the required measurement time and achievable signal-to-noise ratio (S/N) and the effect of a bias cell used in high-resolution molecular photodissocation spectroscopy for the first time. Finally ongoing developments and ideas to improve the quality of our set-up are discussed.

[a)]R. Bejjani and A. Roucou contributed equally to this work. They should be both considered as first author and are placed following the alphabetic order.; Corresponding author: anthony.roucou@uclouvain.be

II. THE TOF-MS AND THE ION SOURCE

The STARGATE instrument is presented in Figure 1. It is essentially composed of a pulsed supersonic expansion coupled to an ionization mean (electric discharge or electron gun). The jet goes through a skimmer, item (2) in Figure 1, which allows for differential pumping and spatial selection of part of the expansion. Ions are then accelerated and enter the TOF-MS. The heart of the TOF-MS includes a single unit, denoted as item (3), able to perform acceleration, bunching, gating of the ionic beam while re-referencing it to the ground potential. The ions are focused using an electrostatic lens (4) and may be deflected using a pulsed deflection unit (5). A second differential pumping (6) is performed before the interaction with a pulsed dye laser and right before entering an energy analyzer (8). The ions are then detected using a microchannel plate stack (MCP, Photonis APD-TOF) and the mass spectra are recorded using a digital oscilloscope (Agilent Technologies DSO-X 3104A, 1 GHz). The timing of the various elements is controlled using a multi-channel digital delay generator (model 577 - BNC) and pulses are generated from Behlke push-pull high voltage (HV) switches. A chronograph of the STARGATE instrument is presented in Figure 2. This figure details the duration and the relative timing of the pulsed jet gas injection (see section II A), the two steps of the gating bunching of the ion beam (see section II D), and the mass selection with the pulsed parallel plate deflector (see section III A).

A. The pulsed supersonic expansion source

The pulsed jet has been chosen as a source of molecules. The motivations for this choice are (i) to promote partial condensation and (ii) to simplify the recorded spectra by increasing the density of molecules on few quantum states and hence increasing the S/N. In order to operate at relatively low pressure (10^{-5} mbar), the pulsed nature of the supersonic expansion was chosen to reduce the pumping requirement for a given gas outflow. A dense and intense, short pulse of gas is produced using a homemade valve based on a flexing disk of piezo material attached to a metallic membrane, as originally developed by Proch and Trickl[27]. Unless specified, a nozzle of diameter of 500 μm has been used with a repetition rate of 30 Hz matching that of the dye laser. A minimum pulse duration of 200 μs has been measured by scanning the gating delay (cfr section II D) of the TOF spectrometer with respect to the valve trigger, and a maximum 1 kHz repetition rate has been obtained. The piezo disk (model P-286.27, Physik Instrumente) is driven by negative 0.3-1.0 kV pulses generated by a home-made push-pull switch whose risetime has been damped by inserting a 511 Ω resistor in series. The fined-threaded aluminum plunger is screwed to the piezo disk and the adjustment of the tightening is made before to place the valve under vacuum. The pulsed duration is controlled by the multi-channel digital delay generator.

B. The ionization methods

The front plate of the nozzle is grounded and the jet starts its expansion at the entrance of an electric discharge. This discharge is produced between a stainless steel circular electrode and the front plate of the nozzle. As illustrated in Figure 3 a), the electrode is surrounded by two circular Teflon insulators and maintained at a negative DC voltage of 0.8 to 1.4 kV. The electric discharge is efficient for ion production but is unstable and runs between the electrode and the plunger of the nozzle instead of the front plate of the valve if the voltage is too high.

Another method to produce ionic species has been implemented with the use of an electron gun to allow more control on the ionization process. The design of this electron gun is based on the work of Hosseinzadeh *et. al.*[28] and is illustrated in Figure 3 b). The electrons are produced by thermionic emission from a thoriated tungsten filament, accelerated by the filament bias voltage, focused towards the supersonic gas jet using side electrodes (-60/-70 V) in Pierce geometry and collected on an electrode placed at a potential of 100 to 500 V.

Most of the results presented in this study were obtained using the electric discharge due to a larger ionic signal. The ionized gas pulse expands towards a conical skimmer of 2 mm diameter. The skimmer allows to spatially select a part of the jet. The vacuum quality is ensured by using three turbo pumps (Pfeiffer ATH 2300M, Balzers 4306, Pfeiffer HiPace 700 Plus) and two stages of differential pumping using the skimmer and a pumping tube indexed as items (2) and (6) in Figure 1, respectively, to finally reach 10^{-7} mbar in the area of the interaction of the ion beam with the laser, the energy analyser and the MCP detector. This allows also to minimize the recombination loss or any warming up by colliding with the residual gas.

C. The extraction

A TOF-MS allows to separate and detect ionized species according to their mass-to-charge ratio m/z[29]. The ions with the same m/z form packets with a specific time of flight t spread by a temporal distribution Δt[29]. In practice for positive ions, a kinetic energy E_k is given by applying an accelerating voltage of -1 kV before the drift tube of the TOF where the ions travel a distance of $d = 1.5$ m before to be detected. Based on simulations made with the SIMION® software, two extraction schemes presented in figures 4 a) and b) have been tested. The first one was inspired from Dedman *et al.*[30] and consists of a series of six aluminum ring electrodes assembled in a tube and connected via voltage divider to produce a smooth gradient of accelerating potential on the ions. The electrodes present successive potentials of 0 V, -200 V, -400 V, -600 V, -800 V and -1000 V and the cations gain kinetic energy from one electrode to the next for a total kinetic energy of 1 keV. The second design is composed of a conical electrode (-700 V) placed 1 cm after the aperture of the grounded skimmer in order to accelerate the ions immediately after the expansion. A succession of two pairs of electrodes at ∼-2 kV and -1 kV allows accelerating the ions on a shorter distance

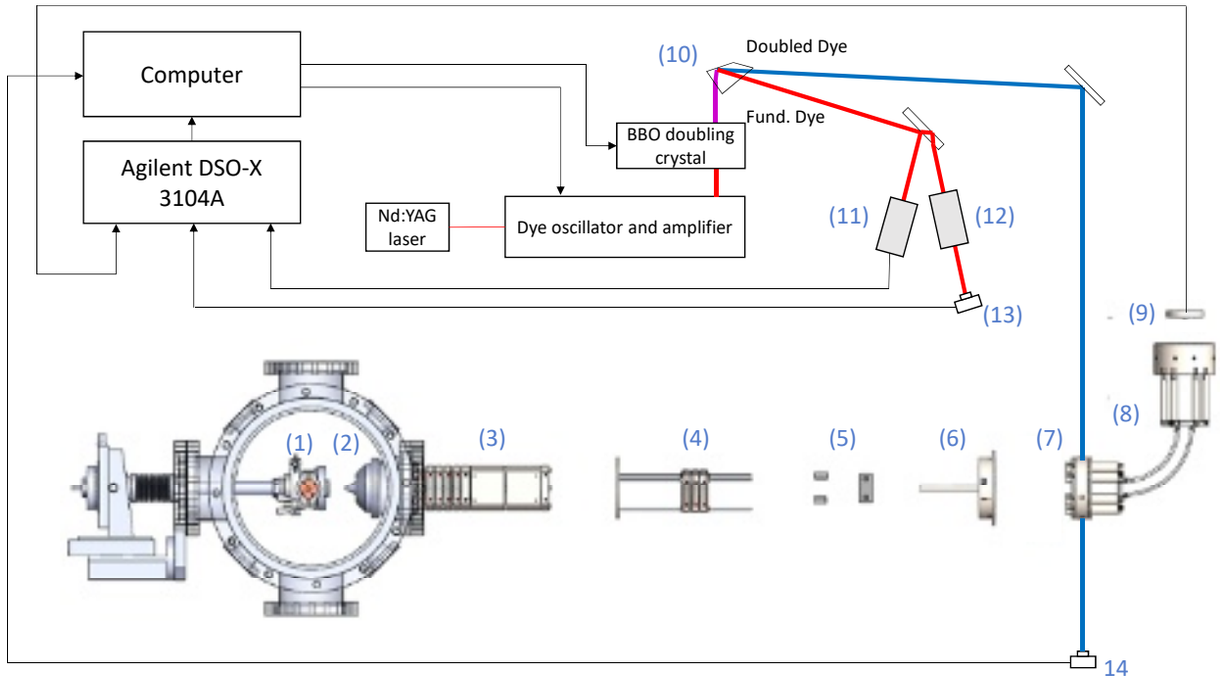

FIG. 1. Design of STARGATE. TOF-MS (bottom) with (1) source of ionic compounds, (2) skimmer, (3) electrostatic extraction and lens coupled to an ion gating, bunching, and re-referencing unit, (4) electrostatic lens, (5) pulsed 2D deflector, (6) differential pumping tube, (7) laser and ion beam interaction region, (8) 90° cylindrical energy analyzer and (9) MCP detector. Optical bench (upper part) with pulsed dye oscillator pumped by a Nd:YAG laser associated with frequency doubler BBO crystal, (10) prism separating the frequency doubled laser (307-327 nm) used for photodissociation spectroscopy from the fundamental dye beam (614-654 nm) used for the frequency calibration of the spectra, (11) hollow cathode, (12) thermalized vaccuum solid state etalon, (13) photodiode and (14) pyroelectric detector (model PE10BB, OPHIR). The calibration Ne optogalvanic spectra (hollow cathode), ionic photofragments (MCP detector) and Fabry Perot interferometer (solid state etalon) are simultaneously measured with an oscilloscope (Agilent DSO-X 3104A) connected to a computer through a USB connector. A Labview^{TM} interface controls the scan of the pulsed dye laser, the transfer of the averaged data from the oscilloscope to the computer, the integration of the time gated signal and the BBO doubling crystal angle for the UV energy pulse optimization. Items (1), (3) and (5) are all connected to a digital delay generator, the associated chronograph is displayed in Figure 2.

and forming an electrostatic lens to focus the ion beam. This second design allowed us to improve the ion signal by at least a factor 30 while keeping a low rotational temperature. The second design has thus been set up permanently and all the results presented in this report were obtained with this extraction scheme.

D. The gating, bunching and re-referencing unit

From what precedes, the accelerated ions are still referenced to the final voltage applied to the extraction column (-1kV in the case of cations). In order to avoid to place the rest of the set-up to high voltage some re-referencing to the ground needs to be set-up. Moreover, the mass resolving power (MRP), $R = m/\Delta m$[31] for a time of flight measurement can be related to the ratio of the time of flight t and the time dispersion Δt of the ions. The uncertainties on t and the magnitude of Δt for species having the same m/z can be decreased by an efficient gating and bunching of the ions, respectively. These three actions, re-referencing, gating and bunching are done by a single unit directly inspired from the work of Dedman *et al.*. The original design leads to a certain mechanical complexity and some specificity for the electronic of the switches[32]. This has been simplified both in terms of mechanics and electronics, during this work, by using only two cup-like electrodes facing one another (instead of 6 plates linked by resistors) denoted A and B in Figures 4 a) and b). These

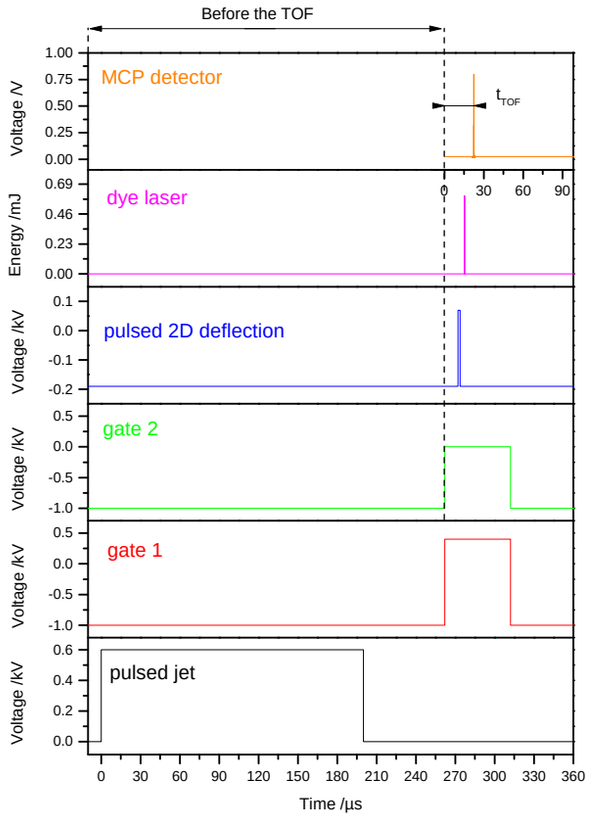

FIG. 2. Chronograph of STARGATE and applied voltages for positive ions. The time scale origin is defined as the rising slope the pulsed molecular jet valve trigger (black). The two steps of the gating bunching of the ions (red and green) and the mass selection of the pulsed 2D deflector (blue) are represented. The time scale origin used for the mass spectrum of N_2O^+ measured with the MCP detector at t_{TOF} =22.4 μs (orange) is defined from the beginning of the TOF corresponding to the gating ($L = 1.5$ m with a kinetic energy of 1 keV). In addition, a dye laser pulse of 5 ns interacts with the ions after 1 m in the drift tube for photodissociation spectroscopy ($\simeq$ 15 μs for N_2O^+).

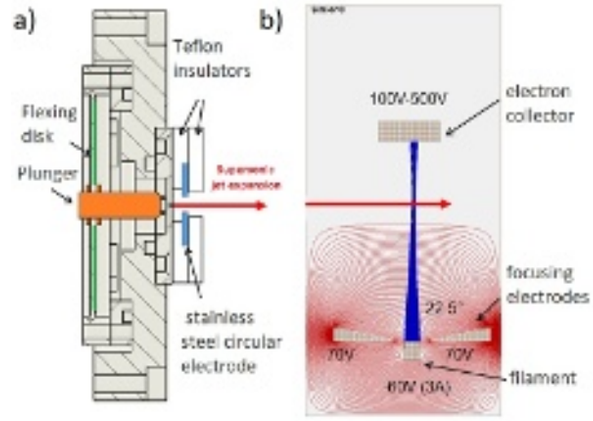

FIG. 3. a) The supersonic jet expansion can be ionized by an electric discharge (800-1400V) produced from a circular electrode (in blue) enclosed in teflon insulators fixed on the valve. The plunger (in orange) is fixed to the flexing disk of piezo material (in green). b) The electron gun scheme is presented with a SIMION® simulation with the electric equipotential lines. The electrons are extracted from a filament (oriented out-of-plane) and accelerated from applied voltage (60 V) and a charged electron collector (100-500V). Two lateral electrodes (-70V) allow to focus the electron beam represented in blue.

are forming a chamber of 83 mm in length and are polarised using conventional push-pull switches. The two steps of the gating bunching process are presented in Figures 4 c) and d) with polarities associated with the study of positive ions. Polarities can of course be reversed for studying negative ions. The gating allows to select a time slice of the ion beam and to define the starting time $t = 0$ for the TOF. The bunching is a longitudinal compression of the ion bunch performed by accelerating the ions lagging behind with a positive potential gradient. Initially, the potential of the two cup electrodes is set to the acceleration voltage (-1 kV) of the extraction to open the first gate (gate 1 in Figure 4 c)) of the unit. The last electrode before the drifting tube is always grounded, the gate 2 is therefore initially closed. When the ion bunch is inside the unit (Figure 4 d)), the electrode A is switched to a positive value ($\sim$400 V) while electrode B is switched to ground after a short and adjustable delay, closing gate 1 and opening gate 2, while excluding the rest of the ion beam and creating a gradient of potential inside the two cup electrodes A and B. This adjustable gradient is used to bunch the ions either at the MCP location or at the crossing with the laser. A tunable delay (40 ns) is introduced between electrodes A and B to further improve the bunching performance of the gating unit by improving the simultaneity of the switches in the two cups. The ions are thus re-referenced at ground potential to propagate in the drift tube and start their flight with a kinetic energy of 1 keV on the right part of the cup electrode B.

The time delay of the gating is controlled by the multichannel digital delay generator and parts A and B of the unit are switched from -1 kV to 400 V and 0 V respectively using two fast HV push-pull switches (rise times of 20 ns). These voltages have been experimentally adjusted and optimized for the bunch of N_2O^+.

Finally, a three-aperture electrostatic lens composed of a biased electrode (650 V) surrounded by two grounded electrodes is placed after this unit to maintain a low spatial divergence of the ion beam in the TOF drift space (item (4) of Figure 1).

E. The mass resolving power

A comparison between the bunched and unbunched signals is presented in Figure 5 for N_2O^+. Ions were produced from a pure expansion of N_2O (stagnation pressure $P = 5$ bar) and an electric discharge (V_d =850 V). The gating selects a time slice of the ion beam (Δt =1.25 μs, i.e. the TOF of N_2O^+ through

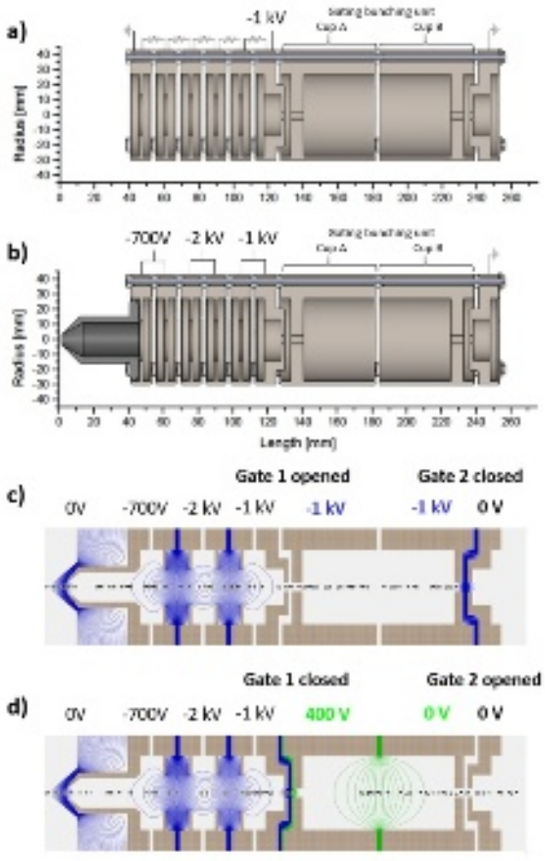

FIG. 4. a) The first acceleration scheme inspired by Dedman *et al.*[30] consisting in a series of six aluminum ring electrodes connected via 100 kΩ resistors to produce a smooth gradient of acceleration potential. b) The second acceleration scheme consisting of the association of a first extraction conical electrode (hole diameter of 6 mm) placed at 1 cm after the grounded skimmer to accelerate and focus the ion beam immediately with a succession of electrodes forming an electrostatic lens. c) The gating process is simulated from SIMION® on the second acceleration scheme using 150 particles of $m = 44$ uma with a charge $+e$ in an initial circular distribution (radius of 1.5 mm and v=550 m/s). The two cup-like electrodes are initially at the acceleration voltage (-1 kV) and a last grounded electrode stops the ion beam reflected in the unit. d) The first part of the unit is switched to +400 V to close the first gate and bunch the ions at the end of the TOF. The second part of the unit is switched to 0 V to let the ions enter the drifting tube. The increment of the electric equipotential lines are 25 V (green) and 30 V (blue) for positive and negative values, respectively.

the gating unit) having a kinetic energy of 1 keV ($v_{N_2O^+} = 66$ km/s) which is compressed to $\Delta t = 80$ ns (FHWM), allowing to observe the $^{14}N^{15}N^{16}O^+$ isotopologue present in natural abundance in the gaseous sample (0.8%). A resulting MRP of $R = 140$ was calculated in the time domain from $R = t_{N_2O^+}/2\Delta t$. The bunching thus improves the MRP and the signal-to-noise by a factor 15 and 8, respectively. Our simple TOF design comes with a loss of MRP of a factor 2 compared to the one reported by Dedman *et. al.*[30].

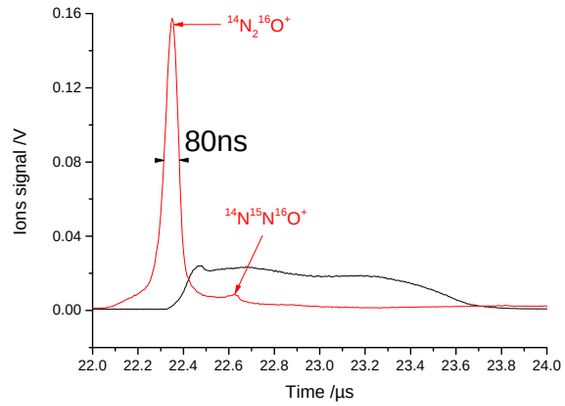

FIG. 5. Comparison between the N_2O^+ m/z bunched (red) and not bunched (black) spectra, the x-axis is the time of flight after the gating. The bunching and the associated improvement of the MRP allows the $^{14}N^{15}N^{16}O^+$ isotopologue to be observed.

F. Production of clusters, cations and anions

STARGATE is designed to produce different ionic species by controlling the initial conditions of the source, such as nozzle geometry, ionization conditions, seeding gas and backing pressure. The first mass spectra of cationic and anionic clusters we have recorded are presented in Figure 6. Large clusters of $H(H_2O)_n^+$ up to $n = 38$ are depicted in panel a). These complexes were produced by the expansion from argon bubbling in a water reservoir. This series stops at n=38 but since the detection efficiency decreases with the mass (lower velocities), larger clusters could be present. Note that the MCP front was negatively biased to 2.1 kV, adding up to 3.1 keV kinetic energy at impact. In panel b) we show the formation of pure $N_2O_n^+$ and mixed $[H_2O_m - N_2O_n]^+$ hydrates clusters formed from N_2O and water contamination in the gas injection pipes. The first steps of nucleation are clearly visible but also the competition between the different routes of nucleation. Anions have also been measured by switching the polarity of the ion optics using the electron gun for ionization of N_2O^+ and replacing the MCP stack with a channel electron multiplier (Sjuts KBL 25 RS) and are presented in panel c) of Figure 6. These three panels illustrate the versatility of STARGATE in terms of molecular targets that could be studied. It also provides evidence of an efficient cooling which will be further demonstrated in Section IV D.

III. PHOTODISSOCIATION SPECTROSCOPY

Photodissociation spectroscopy consists of integrating the ionic fragments signal generated by light absorption of a mass selected ion as a function of the wavelength of a light source, in our case a pulsed dye laser (30 Hz, 0.6 mJ/pulse and 5 ns duration from Continuum ND 6000) pumped by a Nd:YAG laser (Continuum Powerlite Precision II). For this kind of

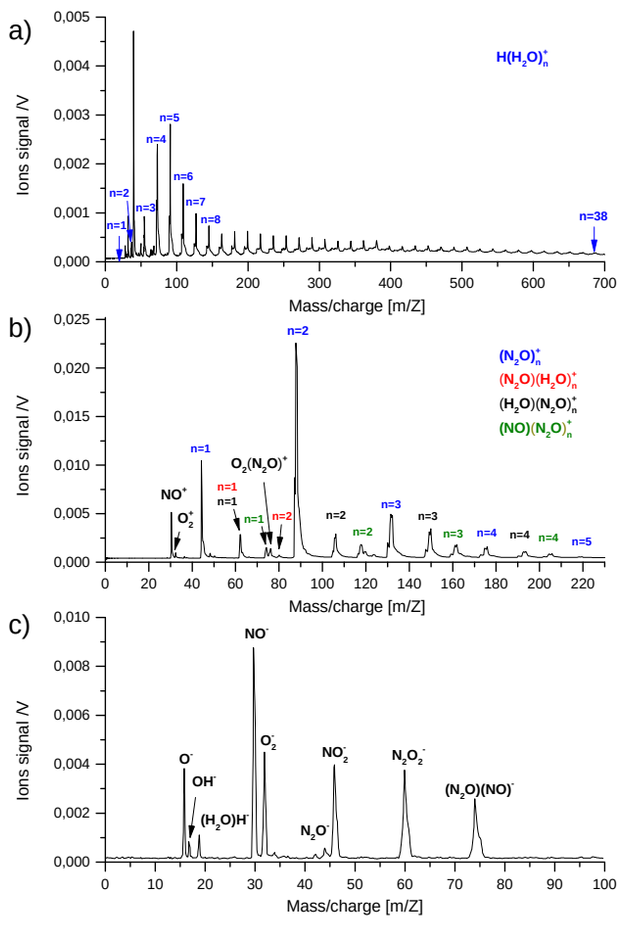

FIG. 6. a) Production of $H(H_2O)_n^+$ ionic clusters up to $n = 38$ from argon bubbling in water with a backing pressure of 2 bar using a nozzle of 1.5 mm with an average pressure of 10^{-5} mbar in the jet chamber and the valve operating at 30 Hz. b) Production of $(N_2O)_n^+$ $(n = 1-5)$, $(N_2O)\cdot(H_2O)_n^+$ $(n = 1-2)$, $(H_2O)\cdot(N_2O)_n^+$ $(n = 1-4)$ and $(NO)\cdot(N_2O)_n^+$ $(n = 1-4)$ ionic clusters from N_2O and residual water in the gas line. c) Production of anions using the electron gun ionization with N_2O with a backing pressure of 2 bar.

measurement to be background free, a selection on the ions has to be performed before and after interaction with the laser. In our case we perform a mass selection, an energy shift at the location of the ion-laser interaction and an energy analysis. In section A hereafter, we detail the pulsed deflection unit we implemented for the first mass selection; in section B the selective energy shifts of the ions produced by the photodissociation and the associated cylindrical energy analyser; and in section C we check the spatial and temporal overlap of the laser with the ions.

A. The first mass selection of ions

The first mass selection is performed using a pulsed 2D deflection to achieve mass-selected absorption measurements. It consists of a pulsed deflector formed by a pair of steering plates to which pulsed voltage is applied to horizontally steer the ion beam towards the laser interaction region and select the species of interest. The mass selection is performed by time-gated deflection using short voltage pulses (typically $\simeq 1\mu$s with 70 V) using a fast HV push-pull switch (risetime of 20 ns) and the multi-channel digital delay generator. A second pair of plates ensures proper vertical alignment. The non-selected ions thus collide with the chamber wall. A comparison of the full m/z spectrum obtained from pure N_2O gas injection with that measured with mass selection applied to select only N_2O^+ is presented in Figure 7.

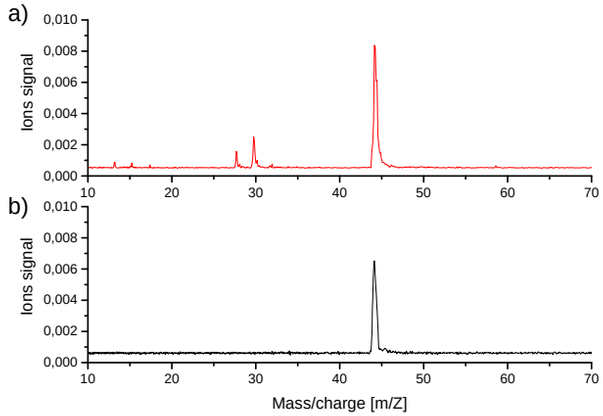

FIG. 7. a) The m/z spectrum measured with continuous deflection from N_2O gas injection and electric discharge (in red) is compared with b) the spectrum measured with a pulsed deflection of 1 μs to select only N_2O^+ (in black).

B. The kinetic energy selection

While the first mass selection selects a species for the laser interaction, other species can result from the collisions of the selected ions with the residual gas in the drift tube. A second selection is performed by a 90° electrostatic deflector after the laser interaction to select the fragments of the photodissociation and to exclude the remaining parent ions and non photo-induced fragments. A double-focusing 90° electrostatic deflector adopting the design of H. Kreckel *et al.*[33] has been implemented for the selection of the fragments depending on their kinetic energy. An electric potential is additionally applied to the laser interaction region by a large cylindrical electrode surrounded by grounded electrodes. This bias cell represented in the left corner of Figure 8 a) aims at increasing the kinetic energy difference between fragments of the photodissociation process, and other fragments or parent molecules. For example, if N_2O^+ has an energy of 1 keV before the bias cell, the fragments NO^+ produced by collisions in the TOF have the same velocity than N_2O^+ but a different mass, their kinetic energy can be calculated to be 680 eV. By polarizing the central electrode (-250 V) of the electrostatic lens

surrounding the laser interaction area (Figure 8 b)), the photodissociation fragments NO^+ are produced from accelerated N_2O^+ having an energy of 1250 eV. With an initial kinetic energy of 852 eV, these fragments are decelerated by leaving the electrostatic lens area to reach a kinetic energy of 602 eV in the 90° electrostatic deflector. This resulting energy is therefore lower than the fragments NO^+ (680 eV) generated outside the interaction region. These fragments can thus be differentiated by tuning the voltages applied on the 90° deflector accordingly. In Figure 8 b), trajectories of N_2O^+, NO^+ produced by collisions outside the bias cell and NO^+ photofragments are represented in blue, red and black, respectively. One can notice in this simulation made using the SIMION® software that all species do not reach the detector except the NO^+ photofragments. We noticed that a similar effect can be observed by switching the voltage to +250 V and tuning the voltage applied on the deflector accordingly.

C. Overlap of the N_2O^+ ion beam with the pulsed dye laser

The S/N of a photodissociation spectrum depends, for the S part, on the amplitude of the NO^+ signal which is integrated and averaged at each frequency step of the laser. The photodissociation signal thus requires maximizing the overlap of the mass-selected ions with the laser beam pulse in the time and spatial domain. The time delay of the pulsed gas injection is thus synchronized with the laser pulse by monitoring the photodissociation fragments on the MCP detector. The overlap of the pulsed laser with the bunched N_2O^+ beam has been evaluated in order to check if the MRP of the TOF-MS (R= 140) is large enough, i.e. Δt small enough compared to the laser pulse duration (5ns). The time delay between the laser and the bunched ion beam has been scanned using the multi-channel digital delay generator. Figure 9 presents the NO^+ fragments generated from N_2O^+ as a function of this delay, with the laser tuned at the Q branch frequency of the $\widetilde{A}^2\Sigma^+(002) \leftarrow \widetilde{X}^2\Pi_{3/2}(000)$ rovibronic band. This scan displays a Gaussian profile of 105 ns FWHM, for a typical laser pulse duration of 5 ns. Nevertheless, most of the ions interact with the laser. Indeed, considering a speed of 66 km/s for an ion of 44 amu ($t_{TOF} \simeq 22\ \mu$s, $E = 1$ keV), a 105 ns dispersion corresponds to an ion bunch length of 6.9 mm which is very close to the diameter of the pulsed laser beam estimated to be ≃6 mm at the interaction region.

IV. APPLICATION TO HIGH RESOLUTION SPECTROSCOPY OF N_2O^+

To evaluate the performances of our spectrometer in terms of frequency accuracy, measuring time, S/N ratio and rotational temperature, the rotationally resolved photodissociation spectrum of N_2O^+ corresponding to the $\widetilde{A}^2\Sigma^+(002) \leftarrow \widetilde{X}^2\Pi_{3/2}(000)$ rovibronic band has been measured several times for different experimental conditions in the UV range by monitoring the apparition of ionic fragments (NO^+) as a function of the laser wavelength. This band has indeed been

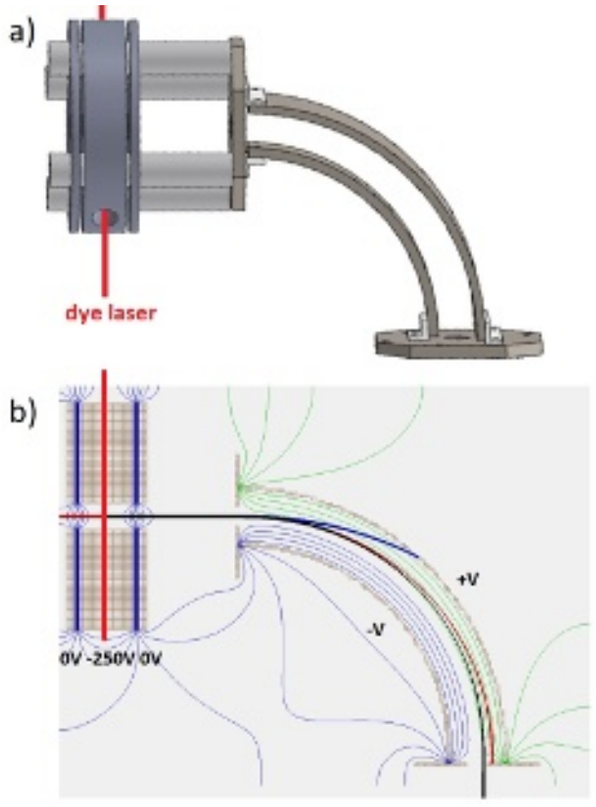

FIG. 8. a) The 90° electrostatic deflector is represented with the bias cell surrounding the laser interaction region. b) SIMION® simulation performed for the selection of the NO^+ photo-fragments ($m = 30$ uma, $E_{NO^+} = 602$ eV) represented in black, by excluding the non-dissociated N_2O^+ parent ions having a larger kinetic energy represented in blue ($m = 44$ uma, $E_{N_2O^+} = 1$ keV) and NO^+ fragments resulting from collisions with the neutral residual gas in the drift tube represented in red ($m = 30$ uma, $E_{NO^+} = 680$ eV). The positive and negative electric equipotential lines are represented in green and blue, respectively, with an increment of 30 V. The voltages applied in the simulation are -250 V for the middle electrode and $\pm V = \pm 135$ V for each plate of the deflector. The initial energy of the photo-fragments is $E_{NO^+} = E_{N_2O^+} \times m_{NO^+}/m_{N_2O^+} = 852$ eV with $E_{N_2O^+} = 1250$ eV in the middle of the electrostatic field generated by the electrostatic lens.

used to evaluate the performances of several spectrometers based on different action type of measurements[34,35]. To use refined molecular parameters of the $\widetilde{A}^2\Sigma^+(002)$ state in the evaluation of our spectrometer, we started by measuring and analysing the $\widetilde{A}^2\Sigma^+(002) \leftarrow \widetilde{X}^2\Pi_{3/2}(000)$ and $\widetilde{A}^2\Sigma^+(002) \leftarrow \widetilde{X}^2\Pi_{1/2}(000)$ rovibronic bands of N_2O^+.

A. The $\widetilde{A}^2\Sigma^+(002) \leftarrow \widetilde{X}^2\Pi(000)$ vibronic band in N_2O^+

The N_2O^+ cation has been extensively investigated in the literature through lifetime measurements[36], optical emission[37–42], photoelectron[43,44] and photodissociation studies[45–54]. The photodissociation of $N_2O^+(\widetilde{A}^2\Sigma^+(002))$ in

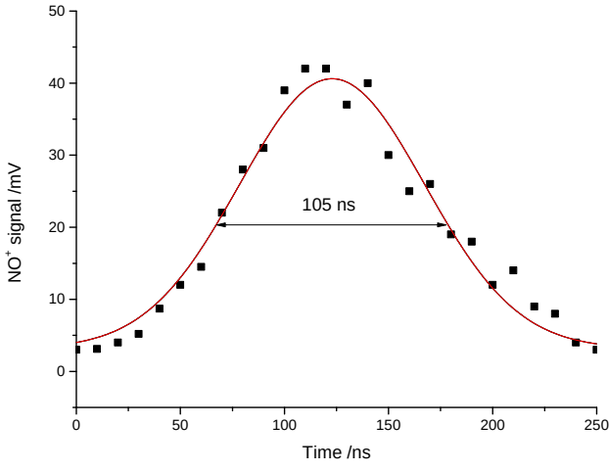

FIG. 9. Laser interaction time profile measured from the NO^+ photofragments by tuning the time delay between the N_2O^+ ion bunch and the laser pulse. The measurements are depicted in black squares and are fitted by a Gaussian profile presented in red. The laser frequency was fixed to the top of the Q branch frequency of the $\widetilde{A}^2\Sigma^+(002) \leftarrow \widetilde{X}^2\Pi_{3/2}(000)$ rovibronic band (30908.5 cm^{-1}). The origin of the x-axis is arbitrary.

the 30885-30940 cm^{-1} range has been experimentally characterized in previous studies[37,51,55] with the following predissociation process :

$$N_2O^+(\widetilde{X}^2\Pi(000)) \xrightarrow{exc.} N_2O^+(\widetilde{A}^2\Sigma^+(002)) \xrightarrow{diss.} NO^+(X^1\Sigma^+) + N(^4S)$$

The $\widetilde{A}^2\Sigma^+(002) \leftarrow \widetilde{X}^2\Pi_{3/2}(000)$ rovibronic band has already been recorded at high resolution[37,46] and is one of the most intense in the 30500-32500 cm^{-1} (307-327 nm) spectral range covered by our frequency doubled pulsed dye laser operating with DCM.

We have used here the convention by Herzberg[42,43], with ν_1 corresponding to the higher frequency N–N σ^+ stretch, ν_2 to the π bend and ν_3 to the lower frequency N–O σ^+ stretch, and not that of Callomon *et al.*[37]. The spectroscopic parameters of the $\widetilde{X}^2\Pi_{3/2}(000)$ ground state have been taken from the work of Fellows *et al.*[39] ($B'' = 0.411601(16)$ cm^{-1}, $D'' = 0.2072(61) \times 10^{-6}$ cm^{-1}, $A'' = -132.3551(11)$ cm^{-1}, $\gamma'' = -0.01424(22)$ cm^{-1}, $p = 0.1385(74) \times 10^{-2}$ cm^{-1} and $q = -0.485(54) \times 10^{-4}$ cm^{-1}). Those of the $\widetilde{A}^2\Sigma^+(002)$ upper state have been firstly taken from Frey *et al.*[46] and improved from analysis of the two intense bands presented in figure 10. A total of 290 line assignments corresponding to 161 blended lines have been fitted with a standard deviation of 0.037 cm^{-1} by least squares methods with PGOPHER[56]. The resulting linelists are presented in table S1 and S2 of Supplementary Informations (SI) and the fitted molecular constants are compared with previous studies in Table I. Comparing with Callomon *et al.*[37], Frey *et al.*[46] and Herburger *et al.*[43], our study allowed to determine the vibronic energy transition $\widetilde{A}^2\Sigma^+(002) \leftarrow \widetilde{X}^2\Pi_{3/2}(000)$ instead of the band head position. A similar analysis also presented in Table I was published very recently by Igosawa et al.[57]. Although their measurements present an accuracy similar to ours, our molecular parameters determination is improved by using the merged blended lines option of PGOPHER. This option takes into account the relative intensities of the transitions in the frequency determination of the merged lines. This improved treatment allowed us to determine the quartic order centrifugal distortion term D'. As detailed hereafter, the $\widetilde{A}^2\Sigma^+(002) \leftarrow \widetilde{X}^2\Pi_{3/2}(000)$ band is used to test the absolute calibration of our measurements, to determine the rotational temperature of the ion beam and to infer the required measurement time to reach a specific signal-to-noise ratio. In the rest of the section, the spectra are compared with the rovibronic simulation calculated with PGOPHER software[56] using the parameters of Fellows *et al.*[39] for the ground state and of Table I for the $\widetilde{A}^2\Sigma^+(002)$ state.

TABLE I. Rovibronic parameters (in cm^{-1}) for the $\widetilde{A}^2\Sigma^+(002)$ excited state. The rotational constantes of the $\widetilde{X}^2\Pi$ ground electronic state have been fixed to the values of Fellows *et al.*[39]. Numbers in parentheses represent 1σ standard deviation in units of the last significant digits.

Parameters	Ref.[37]	Ref.[46]	Ref.[43]	Ref.[57]	This work
ν_0				30844.3(1)	30844.27(10)[a]
B'	0.4290(5)	0.42893(10)	0.4279(8)	0.42891(2)	0.428883(24)
$D' \times 10^7$	1.69(38)	1.6	0.0	1.9	1.89(17)

[a] Value subtracted by 0.1 cm^{-1} (Doppler shift) and standard deviation was calculated from the wavenumber calibration (section IV C for details).

B. Effect of the bias cell

The effect of the bias cell on the photodissociation spectrum of N_2O^+ has been studied. The improvement of the S/N by setting 0 V (DC off) or -250 V (DC on) on the central electrode of the bias cell is presented in Figure 11 a) for the $\widetilde{A}^2\Sigma^+(002) \leftarrow \widetilde{X}^2\Pi_{3/2}(000)$ band. The time-of-flight spectra, recorded for the same laser frequency are also presented in Figure 11, with the bias cell at 0 V in panel c) and -250 V in panel b). On these panels the black traces correspond to the absence of light and the green and blue traces are recorded with the laser on. One can clearly notice in panel b) the separation of the photodissociation fragments from the other fragments produced from collisions in the drift tube. This results in a S/N improved by a factor 4 in the photodissociation spectrum and a removal of the collisional background. The presence of ions generated outside of the laser interaction, observable at 6.5 μs, in panel b), is due to a still too large aperture at the exit of the 90° deflector (hole diameter of 12 mm). These residual ions can be rejected by the selection of a judicious integration time window. The combination of the bias cell and the choice of integration time window ensure thus a background free measurement.

C. Calibration of the frequency scale

The absolute frequency of the photodissociation spectra was calibrated using Ne lines[58] measured from a hollow cathode. This optogalvanic spectrum and the photodissociation

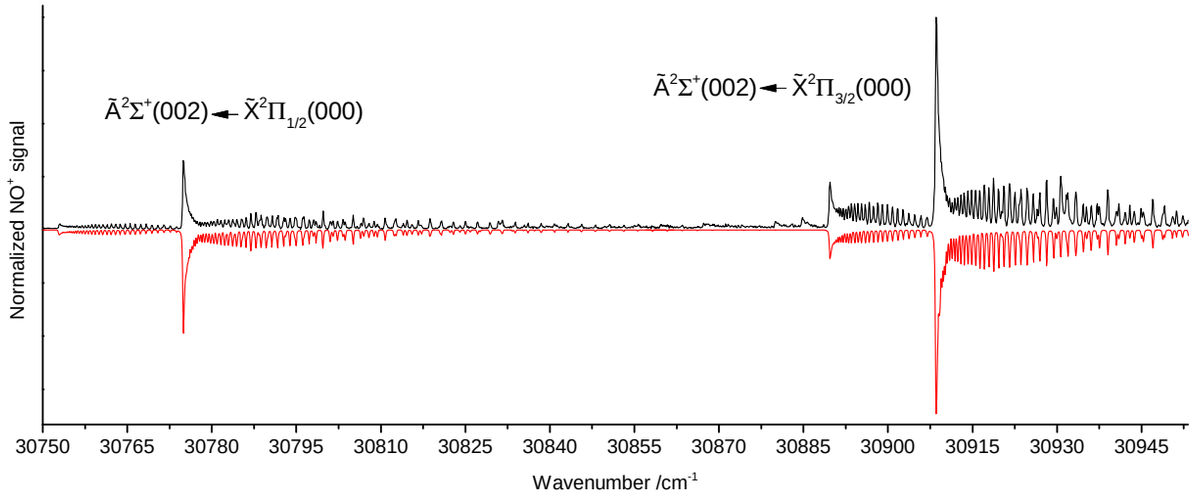

FIG. 10. The photodissociation spectrum (black) has been measured from the interaction of the N_2O^+ beam with a doubled dye laser (0.6 mJ/pulse) for an average of 30 counts per laser step. The simulation (red) was performed with the PGOPHER software[56] using the parameters of Fellows *et al.*[39] for the $\widetilde{X}^2\Pi_{1/2,3/2}(000)$ ground state and those of Table I for the $\widetilde{A}^2\Sigma^+(002)$ state. A temperature of 300 K and a Voigt lineprofile has been considered for the simulation, with Gaussian and Lorentzian contributions of 0.2 cm^{-1} and 0.1 cm^{-1} (FWHM), respectively.

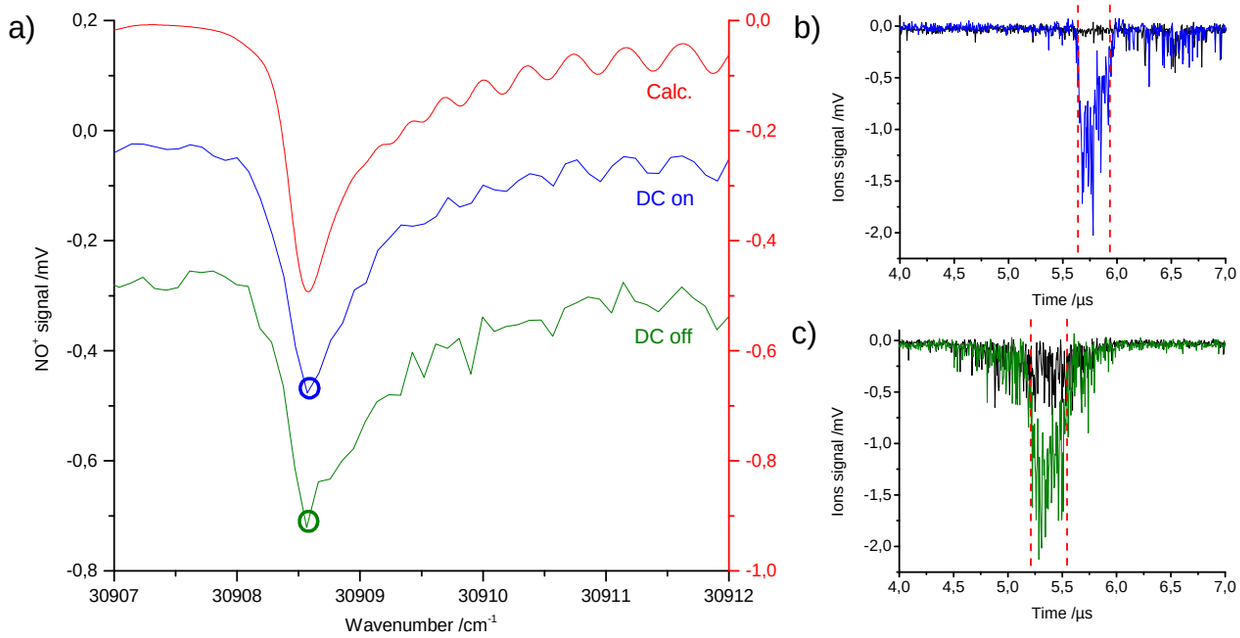

FIG. 11. (a) Q branch region of the $\widetilde{A}^2\Sigma^+(002) \leftarrow \widetilde{X}^2\Pi_{3/2}(000)$ photodissociation spectrum of N_2O^+, from bottom to top measured with the bias cell at 0 V (DC off), at -250 V (DC on) and simulated using the PGOPHER software. The right y-axis used for the calculated spectrum (in red) was scaled on experiment. The experimental ion yields have been shifted vertically for clarity. Blue and green mass spectra of the panels b) and c) are the NO^+ fragments measured at the maximal intensity of the Q branch for the bias cell on and off, respectively. The mass spectra measured without UV laser are presented in black in panels b) and c).

spectrum were simultaneously measured. While the photodissociation spectra have been measured with a frequency doubling BBO crystal in the 307-327 nm spectral range, the atomic Ne lines of the hollow cathode have been measured using the fundamental laser beam (614-654 nm). The absolute calibration of the frequency scale has been performed using

three neon lines (640.40177 nm, 650.83255 nm, 653.46872 nm) with a standard deviation of 0.06 cm^{-1}.

In addition to the absolute calibration, a complementary Fabry Perot interferometer allowed to check the linearity of the laser frequency scanning using a solid state etalon presented in Figure 12 (complete drawings are given in Figure S1-S3 of SI). This interferometer has been designed using an invar ring of 1.99 mm separating two 50:50 beamsplitters enclosed in a thermostatically controlled vacuum chamber (313.0 ± 0.1 K). The resulting Fabry Perot cavity has also been characterized with the fundamental laser beam (614-654 nm) with a free spectral range of 2.507 cm^{-1} and a finesse of 4.4. The residuals of a linear fit performed on the interferences maxima allowed us to check the linearity of the laser frequency scanning with a standard deviation to linearity of 0.014 cm^{-1} and a maximum local deviation value of 0.04 cm^{-1}.

In addition, a Doppler effect arising from a slight deviation from the perpendicular arrangement between the laser and the ion beam has been estimated using a rooftop mirror for a double pass of the laser beam through the ion beam. The double pass spectrum has been reproduced with a linear combination of the single pass spectrum with itself minus 0.2 cm^{-1}. A frequency shift of ± 0.1 cm^{-1} has been thus estimated for each path, this corresponds to a tilt of 0.9° from a perpendicular configuration. Besides this effect which can be corrected by subtracting 0.1 cm^{-1} to the frequency scale, the cumulative errors from relative ($\leq$0.04 cm^{-1}) and absolute (0.06 cm^{-1}) calibrations results in an estimated accuracy of 0.1 cm^{-1} on the calibrated frequency scale.

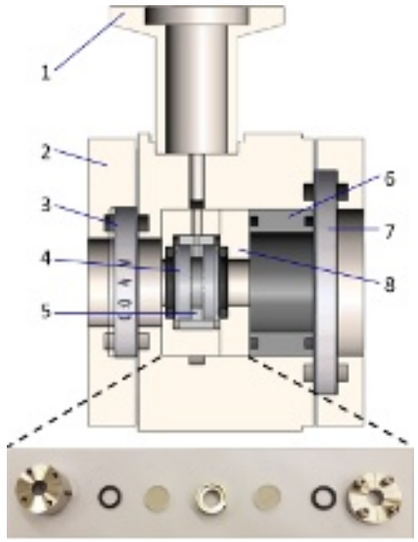

FIG. 12. Fabry Perot etalon composed of: 1) KF fitting for etalon evacuation, 2) external chamber diam. 2″, 3) 1″ wedged window, 4) 50:50 beamsplitters AR coated for 400-700 nm, 5) invar ring of 1.99 mm long, 6) PVC spacer to maintain the position of the stainless steel enclosure in the vacuum chamber, 7) 1.5″ wedge windows and 8) stainless steel enclosure. The exploded view of the etalon and its content is presented below.

D. Rotational temperature

The background free measurement allowed us to measure the selected rovibronic band of N_2O^+ produced from the electric discharge in pure N_2O (P=5 bar) with a $S/N = 200$ and an acquisition average of 30 laser shots per frequency step (this represents one second per frequency step and a time of acquisition of $\simeq$ 10 minutes for each spectrum presented in Figure 13). The rotational temperature can be obtained from a fitting procedure using the PGOPHER software, as well as the Gaussian linewidth and the baseline offset. Experimentally the rotational temperature can be tuned in a certain range by probing different parts of the ion beam using different ion extraction timings and distances between the nozzle and the skimmer. The lowest mean rotational temperature for a pure N_2O expansion (P=3 bar) is 110±4 K and has been obtained using a distance of 1 cm between the skimmer and the nozzle. A maximum mean 305±10 K has been obtained by adding a delay of 12 μs between the gas injection and the gating and by extending the distance between the nozzle and the skimmer to 2 cm. The higher temperature can be obtained from more collisions in the selected part of the jet. These two spectra are presented in Figure 13. It was possible to lower the rotational temperature down to 40±3 K by using a gas mixture of 1% N_2O with 99% Ar and a backing pressure of $P = 5$ bar while probing the early part of the expansion. This spectrum presented in Figure 14 has been measured with a $S/N = 20$ for 30 shots per frequency step. This temperature is smaller by nearly one order of magnitude than the one reported recently by Hirota *et al.* for N_2O^+ using a cryogenic storage ring[35], even for long trapping times.

V. CONCLUSIONS

The versatile STARGATE instrument has been described in this article. The gas injection valve inspired from the work of Proch and Trickl[27] has been associated with a skimmer and an electric discharge or an electron gun to produce isolated or aggregated molecular anions and cations. The extraction, acceleration, bunching/gating and re-referencing of the ionic beam associated with a TOF of $L = 1.5$ m allowed us to reach a R = 140. Two mass selections performed by a parallel plate deflector and a 90° toroidal field deflector associated with an energy tagging of the photodissociation fragments allow to achieve background free rovibronic spectral measurements ($S/N = 200$). The molecular constants in the $\widetilde{A}^2\Sigma^+(002)$ upper state have been improved from the analysis at 300 K of the $\widetilde{A}^2\Sigma^+(002) \leftarrow \widetilde{X}^2\Pi_{3/2}(000)$ and $\widetilde{A}^2\Sigma^+(002) \leftarrow \widetilde{X}^2\Pi_{1/2}(000)$ rovibronic bands. We have demonstrated that the rotational temperatures can be tuned from 40 K to 305 K. The lowest temperature has been obtained using a gas mixture of N_2O (1%) carried by Argon (99%) and by gating the beginning of the ion beam. The higher temperature has been obtained with a pure N_2O gas injection and by delaying gating with respect to the beginning of the gas pulse. This result opens up many perspectives. The lowest temperatures simplify dense rovibronic spectra and increase the S/N by populating fewer

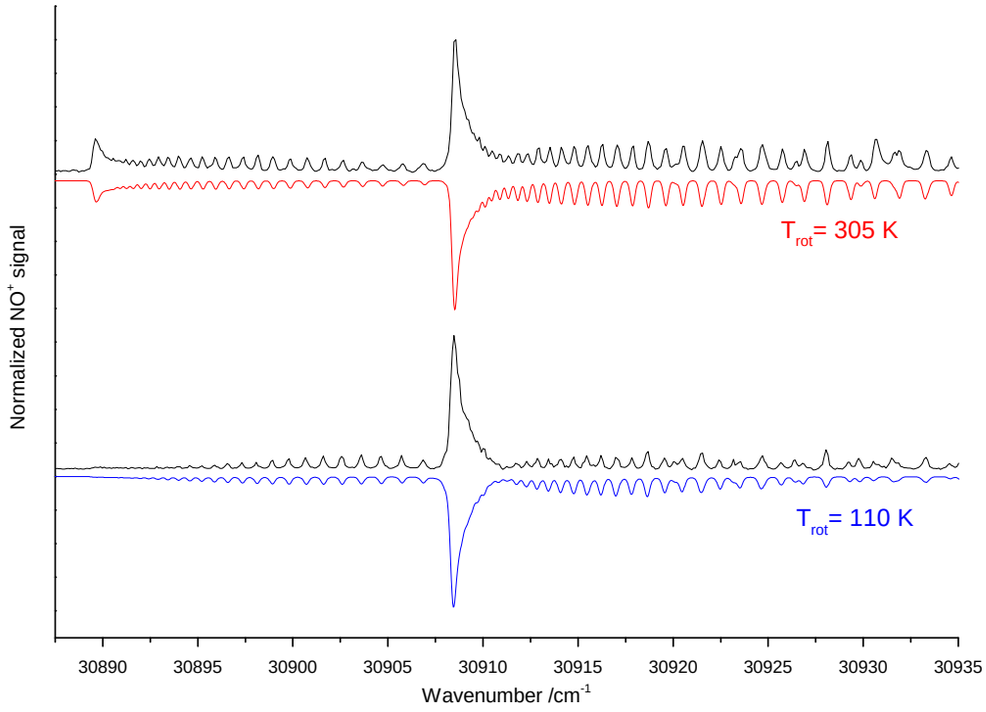

FIG. 13. The photodissociation spectra (black) have been measured from the interaction of the N_2O^+ beam with a doubled dye laser (0.6 mJ/pulse) by probing different part of the ionic beam using different ion extraction timings and distances between the nozzle and the skimmer. An average of 30 counts per laser step allowed to reach a $S/N = 200$ for each spectrum. The simulations have been done for each measured spectrum using the PGOPHER software[56] for T_{rot}=305 K (red) and T_{rot}=110 K (blue).

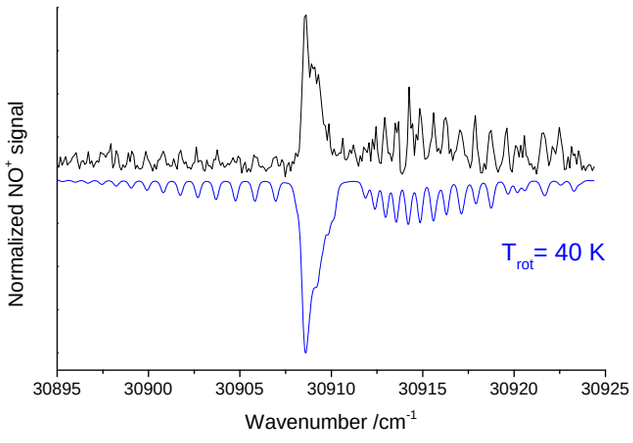

FIG. 14. Photodissociation spectrum (black) measured from a gas mixture of 1% N_2O with 99%Ar (P=5 bar). The simulation (blue) have been done using the PGOPHER software[56] for T_{rot}=40 K.

quantum states and may be used to promote partial condensation. The ability to produce higher temperature ions allows to observe transitions associated with larger total angular momentum J values and hot vibrational bands for small molecular ions (3-4 atoms). Thus, additional information on the dynamics of the molecule can be extracted and additional lines can be assigned to help detecting molecular ions in relatively hot environments.

Concerning the possible improvements of our set-up, the pulsed supersonic expansion could be improved by reducing the residual pressure in the extraction unit and in the drift tube, thereby limiting the number of detrimental collisions of the ions with the residual gas. Moreover we have noticed a lack of stability in the design of Proch and Trickl[27] after a few hours of operation with an electric discharge. We thus plan to build a faster valve based on the design of A. Catanese *et al.*[59] in a near future, preferably used in combination with the electron gun. Shorter pulses are promising in terms of density, temperature and also since only 1.25 μs of the ion beam duration (for 1 keV N_2O^+) is selected by the gating bunching unit compared to 200 μs of pulsed gas injection. Furthermore, following the results of preliminary SIMION® simulations, the MRP of our simplified TOF set-up could be improved by using shorter cups. Finally, the sensitivity of the spectrometer could be ameliorated further by using a post acceleration of the ions[60] between the 90° energy analyzer and the MCP detector as to increase the MCP detection efficiency[61].

SUPPLEMENTARY MATERIAL

See supplementary material for the resulting linelists of N_2O^+ and the drawings of the solid state etalon.

DATA AVAILABILITY STATEMENT

The data that support the findings of this study are available from the corresponding author upon reasonable request.

ACKNOWLEDGMENTS

We are gratefull to Pr. Michel Herman (Université Libre de Bruxelles, ULB) and Pr. Arnaud Delcorte (Université Catholique de Louvain, UCLouvain) for their useful comments and discussions. This project has been funded by the Action de Recherches Concertées (ARC iBEAM-18/23-090) and the Fonds de la Recherche Scientifique - FNRS under grant number J.0179.18, J.0129.20 and IISN grant, number 4.4504.10. XU is a Senior Research Associate of the Fonds de la Recherche Scientifique - FNRS. We also thank the Wallonie-Bruxelles International excellence fellowship (session 2019) for partly funding the post-doctoral research stay of AR.

[1] H. Andrä, in *Progress in Atomic Spectroscopy* (Springer, 1979) pp. 829–953.
[2] M. Carré, M. Druetta, M. Gaillard, H. Bukow, M. Horani, A. Roche, and M. Velghe, Mol. Phys. **40**, 1453–1480 (1980).
[3] H. A. Schwarz, J. Chem. Phys. **67**, 5525–5534 (1977).
[4] M. Okumura, L. Yeh, and Y.-T. Lee, in *Laser Spectroscopy VII* (Springer, 1985) pp. 122–125.
[5] M. Okumura, L. Yeh, J. Myers, and Y.-T. Lee, J. Chem. Phys. **85**, 2328–2329 (1986).
[6] J. M. Lisy, J. Chem. Phys. **125**, 132302 (2006).
[7] M. White, R. Rosenberg, G. Gabor, E. Poliakoff, G. Thornton, S. Southworth, and D. Shirley, Review of Scientific Instruments **50**, 1268–1273 (1979).
[8] J. Lemaire, P. Boissel, M. Heninger, G. Mauclaire, G. Bellec, H. Mestdagh, A. Simon, S. Le Caer, J. Ortega, F. Glotin, *et al.*, Physical Review Letters **89**, 273002 (2002).
[9] L. Yeh, M. Okumura, J. Myers, J. Price, and Y. Lee, The Journal of chemical physics **91**, 7319–7330 (1989).
[10] T. G. Dietz, M. A. Duncan, D. E. Powers, and R. E. Smalley, The Journal of Chemical Physics **74**, 6511–6512 (1981).
[11] K. LaiHing, R. Wheeler, W. Wilson, and M. Duncan, The Journal of chemical physics **87**, 3401–3409 (1987).
[12] J. B. Fenn, M. Mann, C. K. Meng, S. F. Wong, and C. M. Whitehouse, Science **246**, 64–71 (1989).
[13] M. F. Bush, J. T. O'Brien, J. S. Prell, R. J. Saykally, and E. R. Williams, J. Am. Chem. Soc. **129**, 1612–1622 (2007).
[14] A. Osterwalder, M. J. Nee, J. Zhou, and D. M. Neumark, J. Chem. Phys. **121**, 6317–6322 (2004).
[15] E. J. Bieske and O. Dopfer, Chem. Rev. **100**, 3963–3998 (2000).
[16] O. Asvany, E. Hugo, F. Müller, F. Kühnemann, S. Schiller, J. Tennyson, and S. Schlemmer, J Chem. Phys. **127**, 154317 (2007).
[17] S. Chakrabarty, M. Holz, E. K. Campbell, A. Banerjee, D. Gerlich, and J. P. Maier, J. Phys. Chem. Lett. **4**, 4051–4054 (2013).
[18] E. K. Campbell, M. Holz, D. Gerlich, and J. P. Maier, Nature **523**, 322–323 (2015).
[19] O. Asvany, K. M. Yamada, S. Brünken, A. Potapov, and S. Schlemmer, Science **347**, 1346–1349 (2015).
[20] C. E. Dessent and K. Müller-Dethlefs, Chem. Rev. **100**, 3999–4022 (2000).
[21] C. Lauzin, U. Jacovella, and F. Merkt, Mol. Phys. **113**, 3918–3924 (2015).
[22] U. Jacovella, C. J. Stein, M. Grütter, L. Freitag, C. Lauzin, M. Reiher, and F. Merkt, Phys. Chem. Chem. Phys. **20**, 1072–1081 (2018).
[23] D. M. Neumark, Accounts Chem. Res. **26**, 33–40 (1993).
[24] H. S. Biswal, Y. Loquais, B. Tardivel, E. Gloaguen, and M. Mons, J. Am. Chem. Soc. **133**, 3931–3942 (2011).
[25] I. Dyukova, E. Carrascosa, R. P. Pellegrinelli, and T. R. Rizzo, Anal. Chem. (2020).
[26] C. J. Gray, B. Schindler, L. G. Migas, M. Picmanova, A. R. Allouche, A. P. Green, S. Mandal, M. S. Motawia, R. Sanchez-Perez, N. Bjarnholt, *et al.*, Anal. Chem. **89**, 4540–4549 (2017).
[27] D. Proch and T. Trickl, Rev. Sci. Instrum. **60**, 713–716 (1989).
[28] M. Hosseinzadeh and A. Sadighzadeh, "Design and numerical simulation of thermionic electron gun," arXiv preprint arXiv:1509.06363 (2015).
[29] R. J. Cotter (ACS Publications, 1994).
[30] C. Dedman, E. Roberts, S. Gibson, and B. Lewis, Rev. Sci. Instrum. **72**, 2915–2922 (2001).
[31] A. D. McNaught, A. Wilkinson, *et al.*, *Comp. Chem. Term.*, Vol. 1669 (Blackwell Science Oxford, 1997).
[32] C. Dedman, E. Roberts, S. Gibson, and B. Lewis, "Fast 1 kv metal-oxide-semiconductor field-effect transistor switch," Review of Scientific Instruments **72**, 3718–3720 (2001).
[33] H. Kreckel, H. Bruhns, K. Miller, E. Wåhlin, A. Davis, S. Höckh, and D. Savin, Rev. Sci. Instrum. **81**, 063304 (2010).
[34] A. Dzhonson, D. Gerlich, E. J. Bieske, and J. P. Maier, J. Mol. Struct. **795**, 93–97 (2006).
[35] A. Hirota, R. Igosawa, N. Kimura, S. Kuma, K. Chartkunchand, P. Mishra, M. Lindley, T. Yamaguchi, Y. Nakano, and T. Azuma, Physical Review A **102**, 023119 (2020).
[36] D. Klapstein and J. P. Maier, Chem. Phys. Lett. **83**, 590–593 (1981).
[37] J. H. Callomon and F. Creutzberg, Philos. Tr. R. Soc. S.-A. **277**, 157–189 (1974).
[38] C. E. Fellows and M. Vervloet, Chem. Phys. **264**, 203–209 (2001).
[39] C. Fellows, J. Chem. Phys. **138**, 164316 (2013).
[40] L. Lessa, A. Martins, C. Fellows, *et al.*, J. Chem. Phys. **143** (2015).
[41] L. Lessa, S. de Cândido, and C. Fellows, J. Chem. Phys. **140**, 214311 (2014).
[42] M. A. Gharaibeh and D. J. Clouthier, J. Chem. Phys. **136**, 044318 (2012).
[43] H. Herburger, U. Hollenstein, J. A. Agner, and F. Merkt, J. Chem. Phys. **151**, 144302 (2019).
[44] W. Chen, J. Liu, and C. Ng, J. Phys. Chem. A **107**, 8086–8091 (2003).
[45] R. G. Orth and R. C. Dunbar, J. Chem. Phys. **66**, 1616–1620 (1977).
[46] R. Frey, R. Kakoschke, and E. Schlag, Chem. Phys. Lett. **93**, 227–231 (1982).
[47] M. Larzilliere and C. Jungen, Mol. Phys. **67**, 807–837 (1989).
[48] T. F. Thomas, F. Dale, and J. F. Paulson, J. Chem. Phys. **67**, 793–800 (1977).
[49] M. Larzillière, S. Abed, M. Carré, M. Gaillard, J. Lermé, and M. Broyer, Chem. Phys. Lett. **119**, 55–60 (1985).
[50] H. Xu, Y. Guo, Q. Li, S. Liu, X. Ma, J. Liang, and H. Li, J. Chem. Phys. **119**, 11609–11614 (2003).
[51] H. Xu, Y. Guo, Q. Li, Y. Shi, S. Liu, and X. Ma, J. Chem. Phys. **121**, 3069–3073 (2004).
[52] S. Abed, M. Broyer, M. Carre, M. Gaillard, and M. Larzilliere, Chem. Phys. **74**, 97–112 (1983).
[53] M. Larzilliere, M. Carre, M. L. Gaillard, J. Rostas, M. Horani, and M. Velghe, J. Chim. Phys. **77**, 689–693 (1980).
[54] Z. Zhou, H. Liang, Z. Hua, S. Feng, D. Zhao, and Y. Chen, J. Chem. Phys. **150**, 226101 (2019).
[55] H. Wang, X. Zhou, S. Liu, B. Jiang, D. Dai, and X. Yang, J. Chem. Phys. **132**, 244309 (2010).
[56] C. M. Western, J. Quant. Spectrosc. Ra. **186**, 221–242 (2017).
[57] R. Igosawa, A. Hirota, N. Kimura, S. Kuma, K. Chartkunchand, P. Mishra, M. Lindley, T. Yamaguchi, Y. Nakano, and T. Azuma, J. Chem. Phys. **153**, 184305 (2020).
[58] "Nist atomic spectra database," `https://physics.nist.gov/PhysRefData/ASD/lines_form.html`.
[59] A. Catanese, S. Horton, Y. Liu, and T. Weinacht, Rev. Sci. Instrum. **89**, 103115 (2018).

[60]J. Gibbard, A. Shin, E. Castracane, and R. Continetti, Rev. Sci. Instrum. **89**, 123304 (2018).

[61]R. Liu, Q. Li, and L. M. Smith, J. Am. Soc. Mass. Spectr. **25**, 1374–1383 (2014).

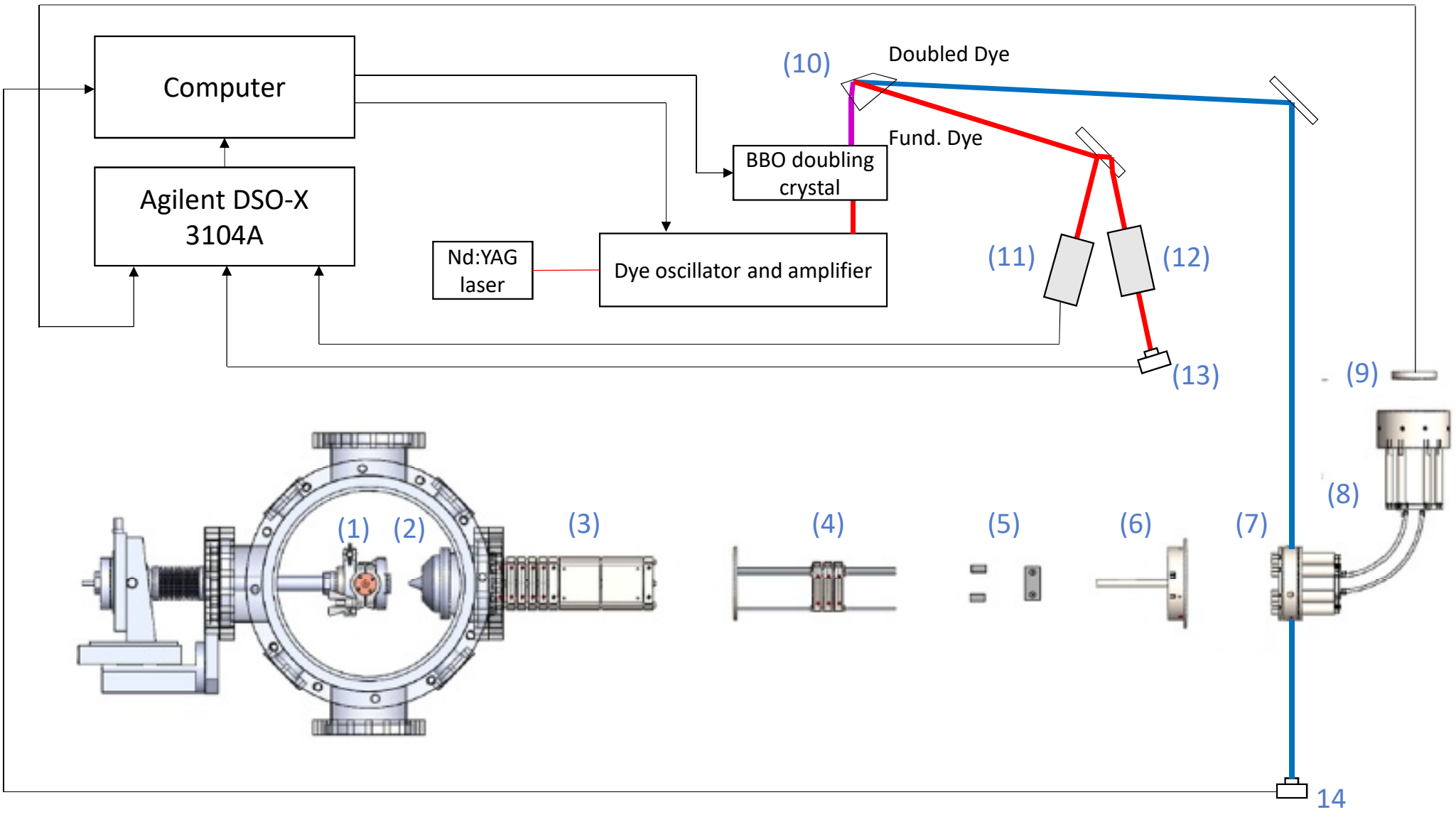
Computer
Agilent DSO-X 3104A
Nd:YAG laser
Dye oscillator and amplifier
BBO doubling crystal
(10)
Doubled Dye
Fund. Dye
(11)
(12)
(13)
(9)
(8)
(1)
(2)
(3)
(4)
(5)
(6)
(7)
14

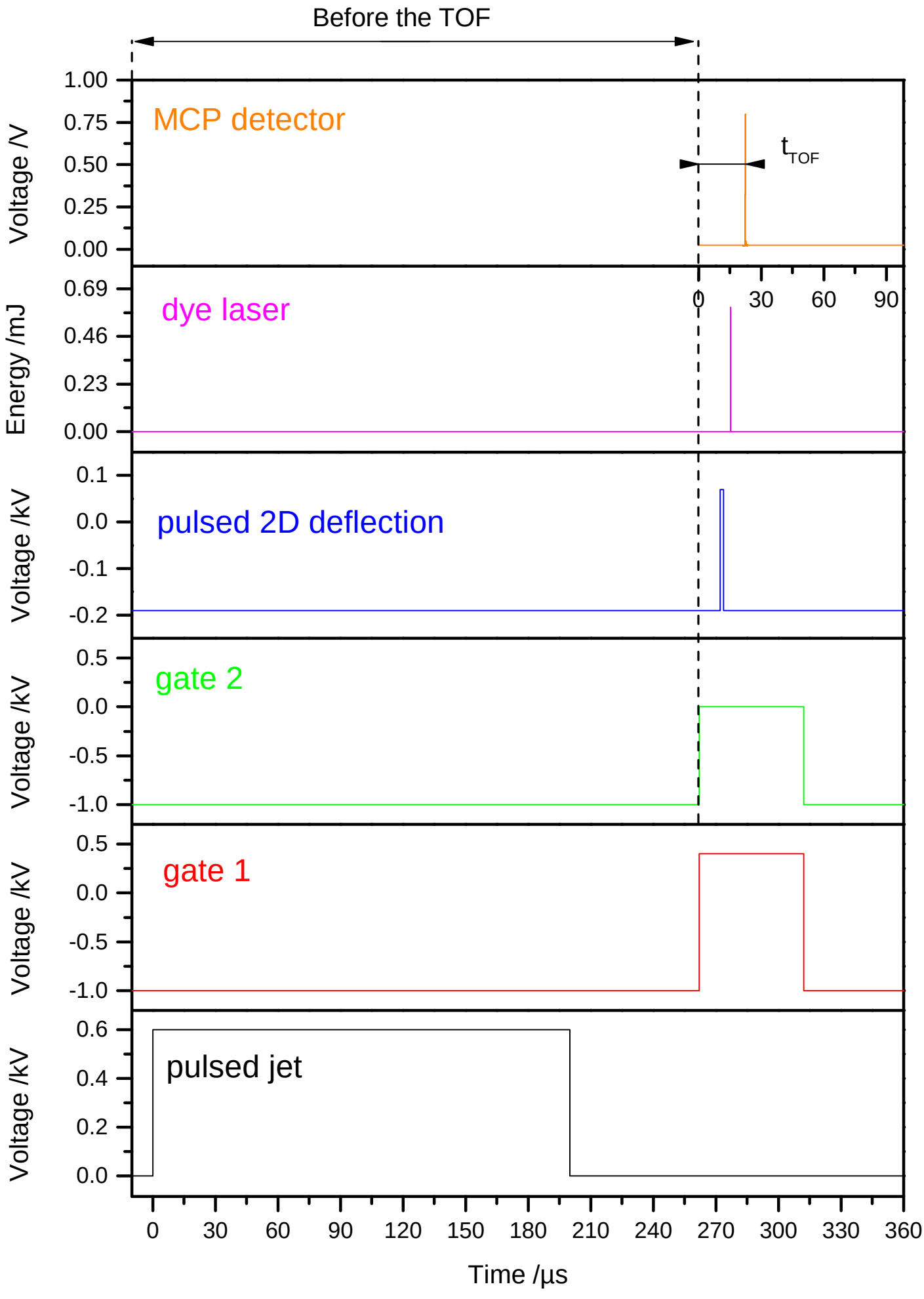
Before the TOF
MCP detector
t_{TOF}
Voltage /V
1.00
0.75
0.50
0.25
0.00
dye laser
Energy /mJ
0.69
0.46
0.23
0.00
0
30
60
90
pulsed 2D deflection
Voltage /kV
0.1
0.0
-0.1
-0.2
gate 2
Voltage /kV
0.5
0.0
-0.5
-1.0
gate 1
Voltage /kV
0.5
0.0
-0.5
-1.0
pulsed jet
Voltage /kV
0.6
0.4
0.2
0.0
0
30
60
90
120
150
180
210
240
270
300
330
360
Time /µs

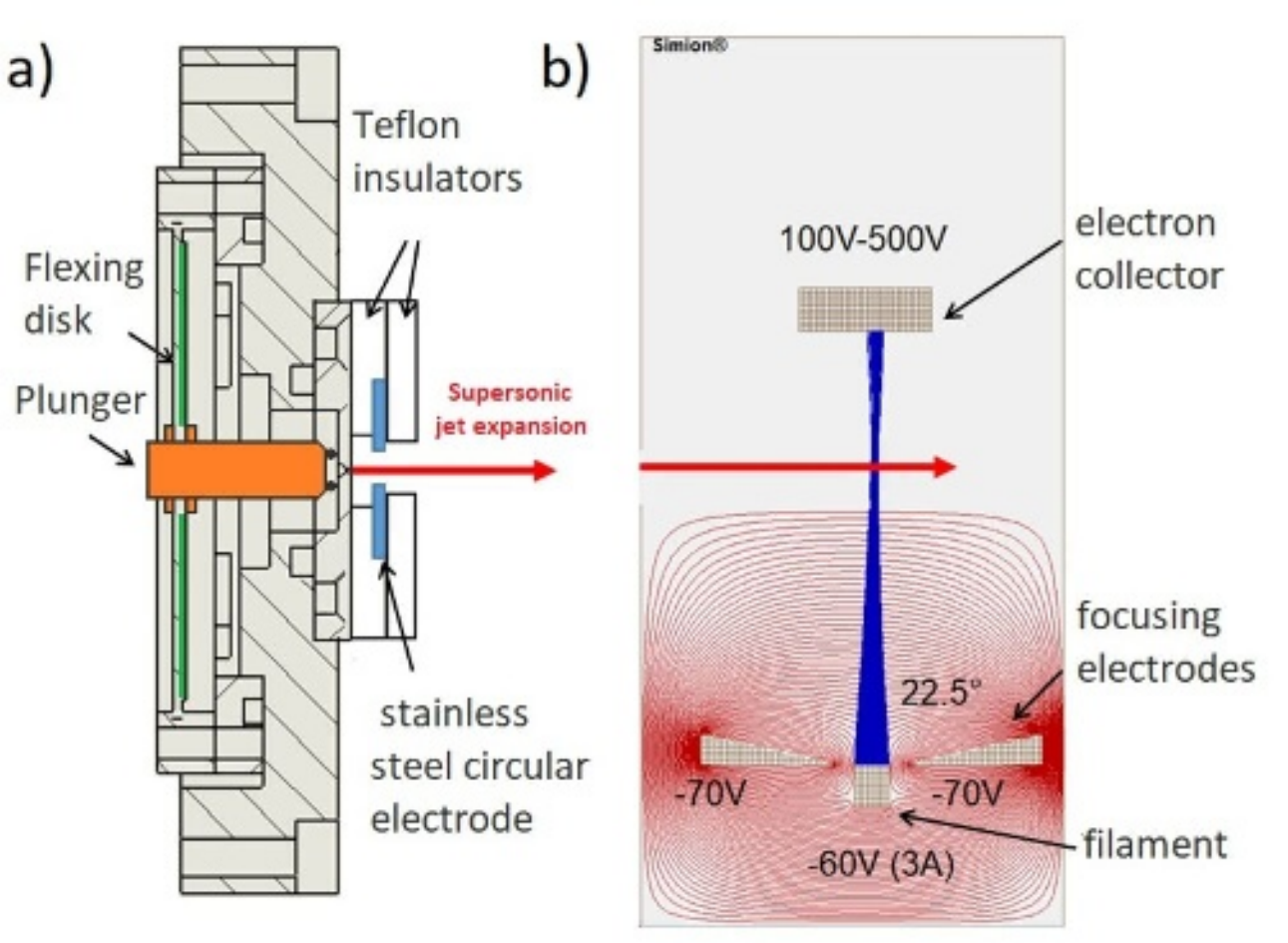
a)
Teflon
insulators
Flexing
disk
Plunger
Supersonic
jet expansion
stainless
steel circular
electrode
b)
Simion®
100V-500V
electron
collector
focusing
electrodes
22.5°
-70V
-70V
filament
-60V (3A)

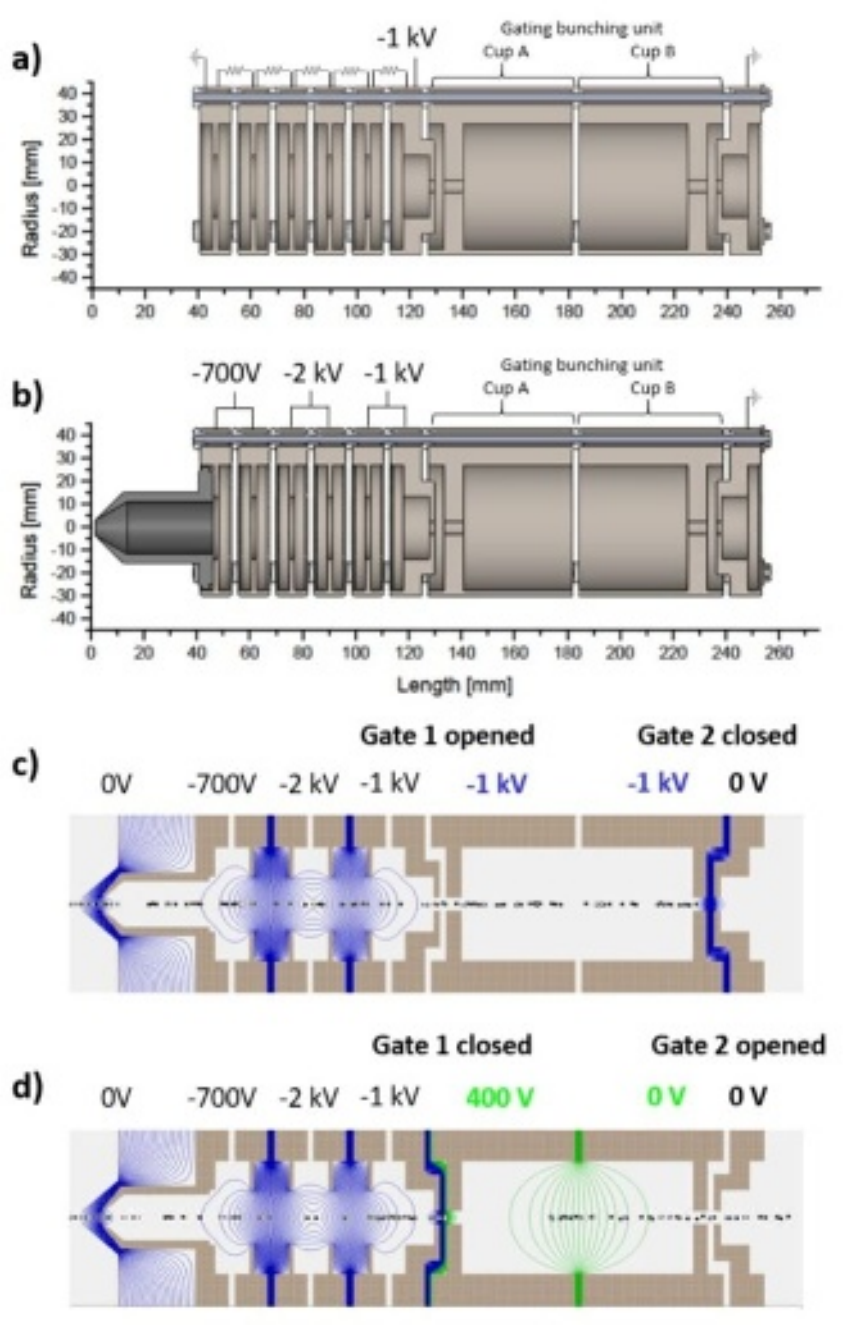
a)
-1 kV
Gating bunching unit
Cup A
Cup B
Radius [mm]
b)
-700V
-2 kV
-1 kV
Gating bunching unit
Cup A
Cup B
Radius [mm]
Length [mm]
c)
Gate 1 opened
Gate 2 closed
0V
-700V
-2 kV
-1 kV
-1 kV
-1 kV
0 V
d)
Gate 1 closed
Gate 2 opened
0V
-700V
-2 kV
-1 kV
400 V
0 V
0 V

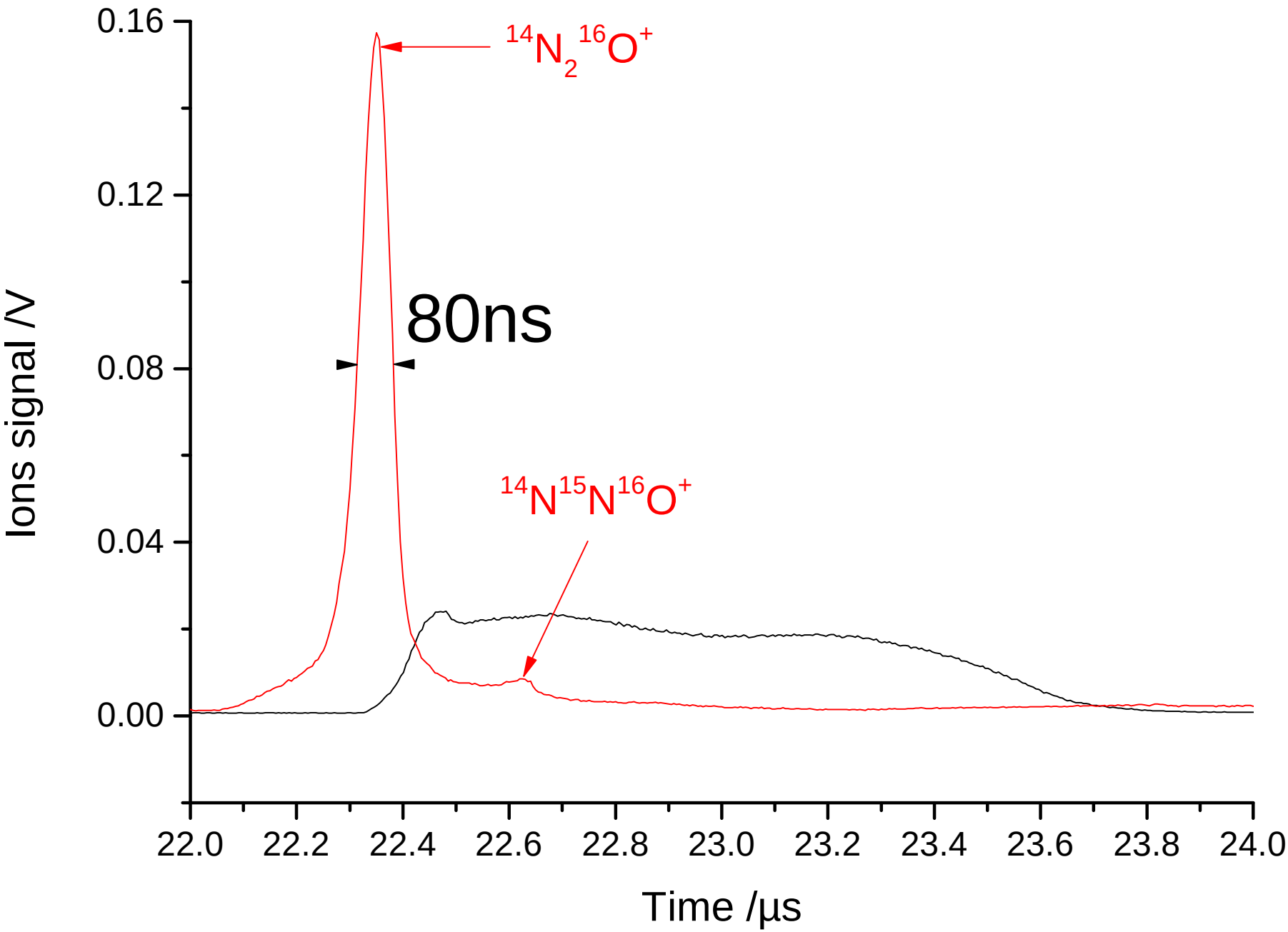
0.16
0.12
0.08
0.04
0.00
Ions signal /V
$^{14}N_2{}^{16}O^+$
80ns
$^{14}N^{15}N^{16}O^+$
22.0
22.2
22.4
22.6
22.8
23.0
23.2
23.4
23.6
23.8
24.0
Time /μs

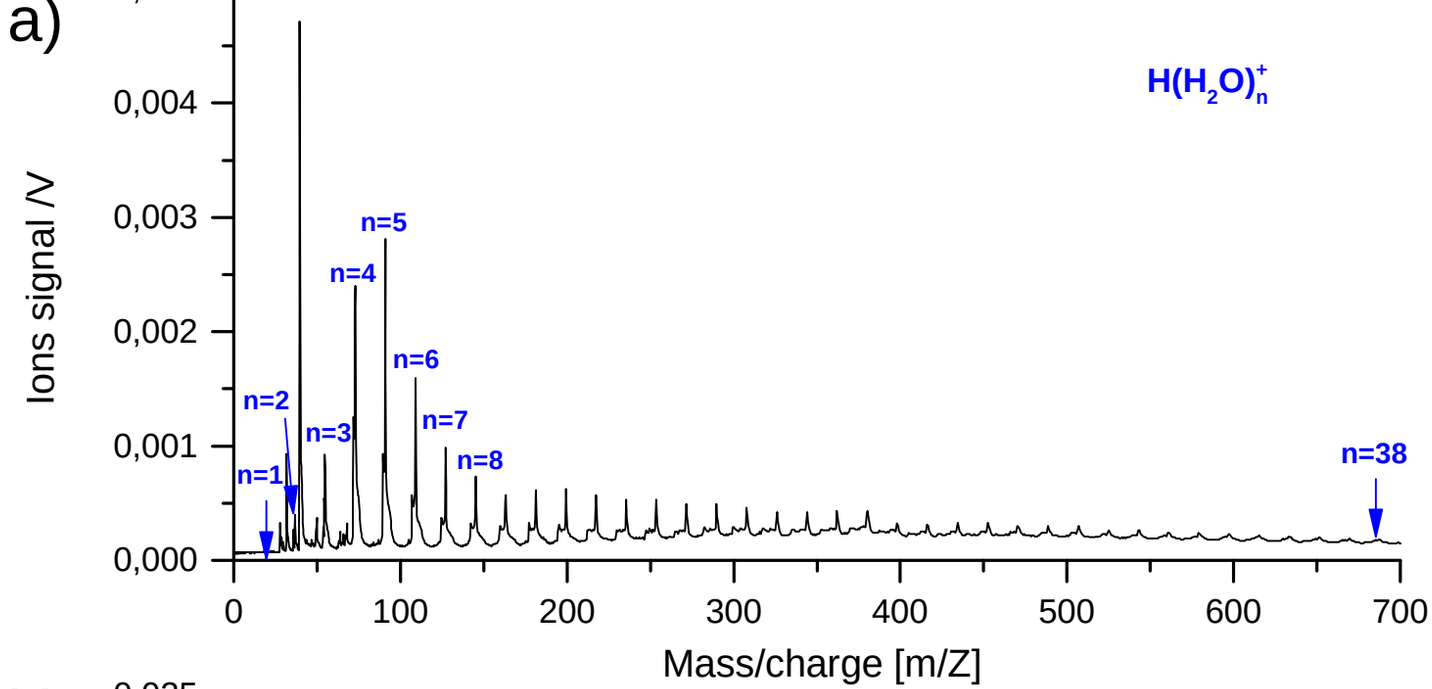

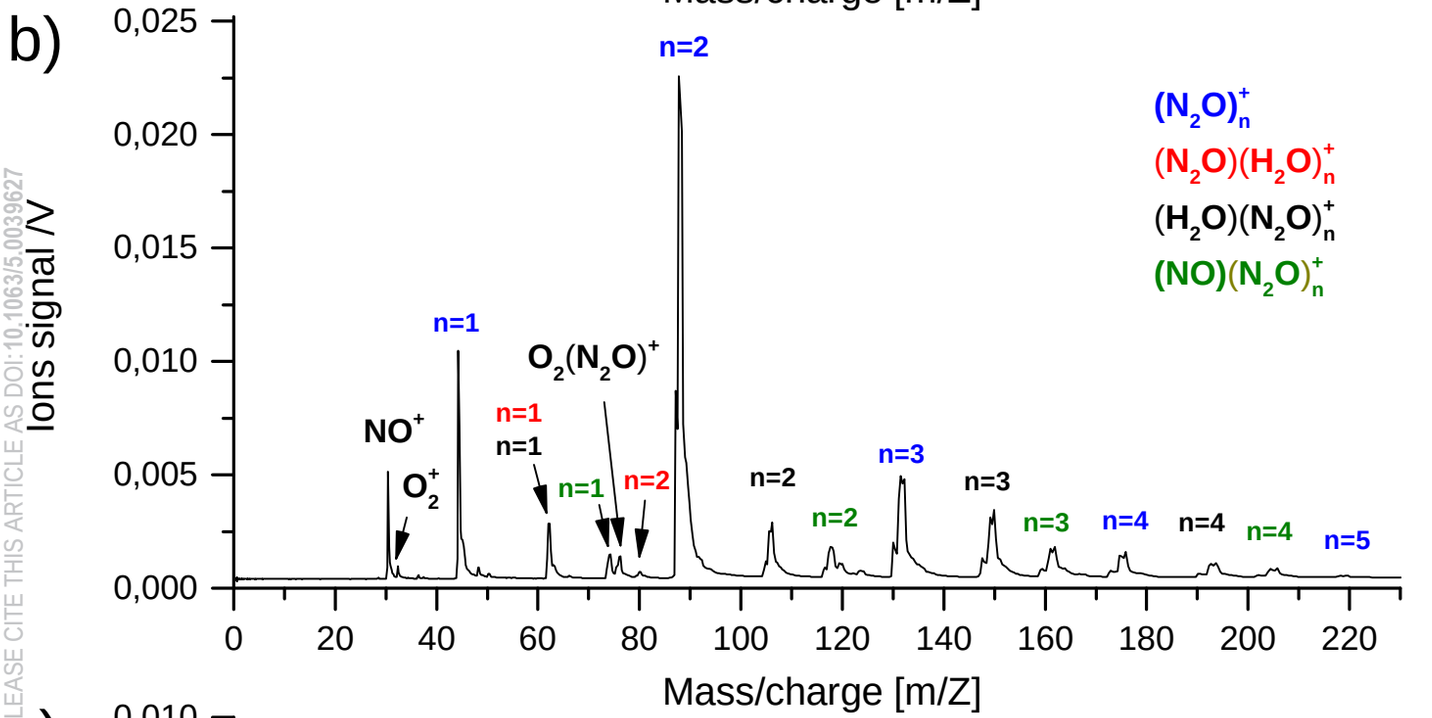

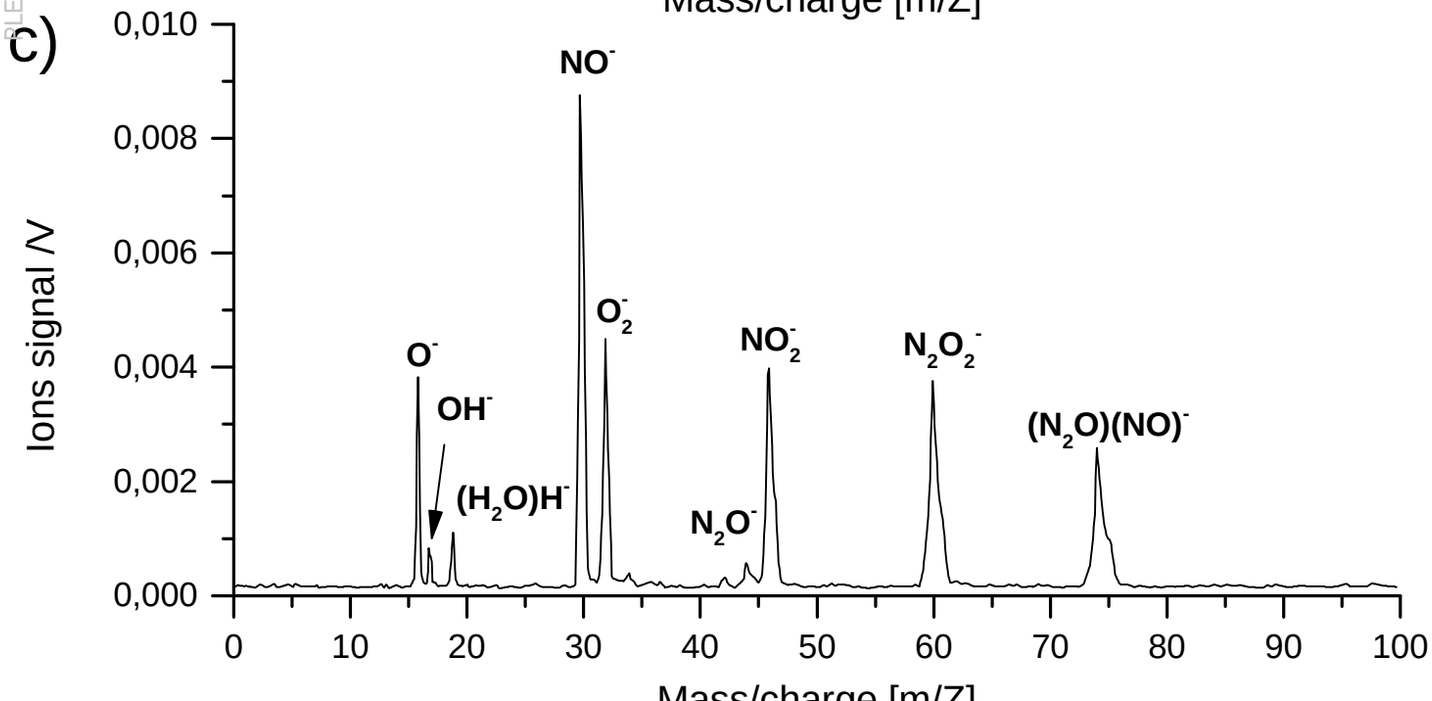

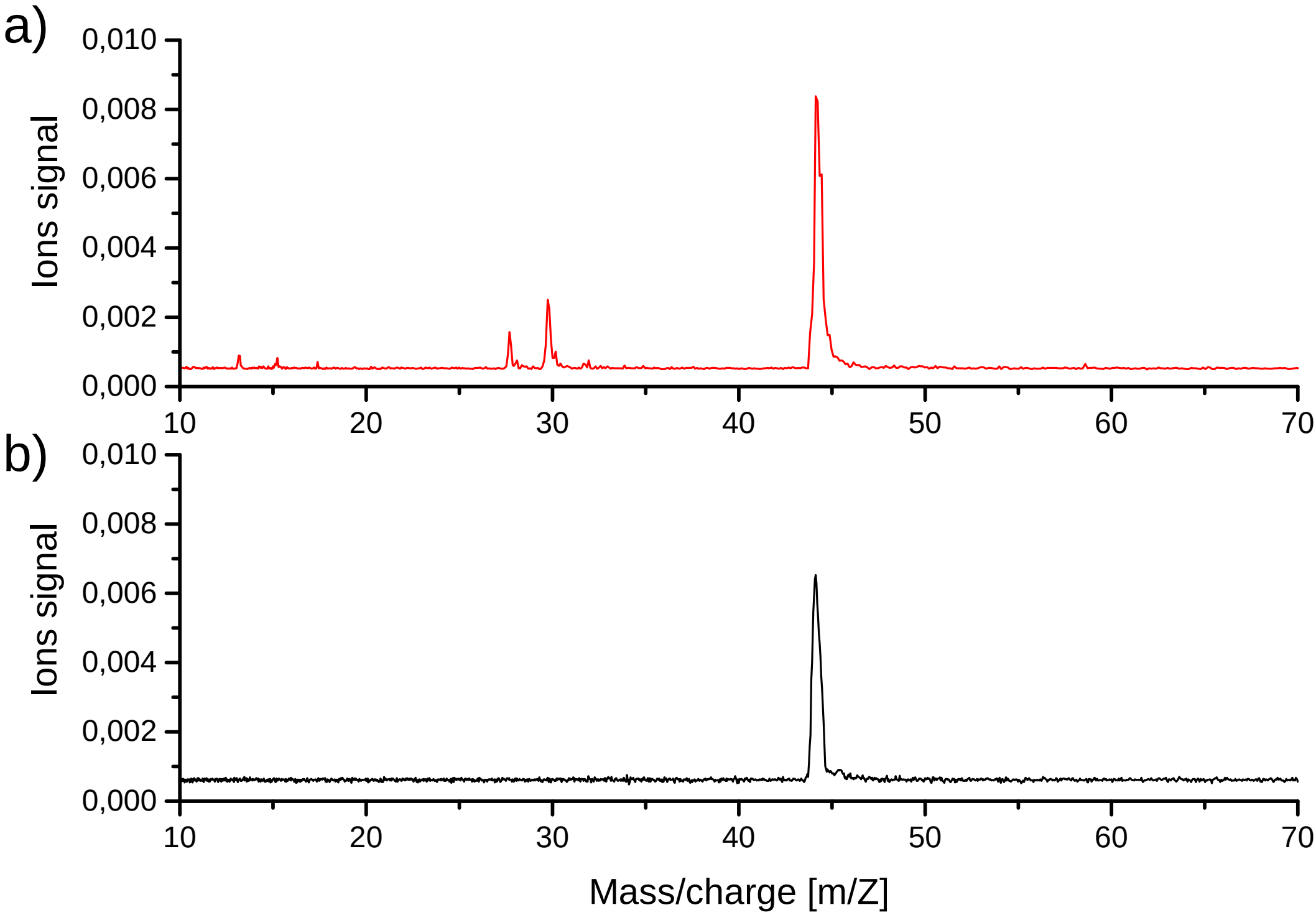
a)
b)
Ions signal
0,010
0,008
0,006
0,004
0,002
0,000
10
20
30
40
50
60
70
Mass/charge [m/Z]

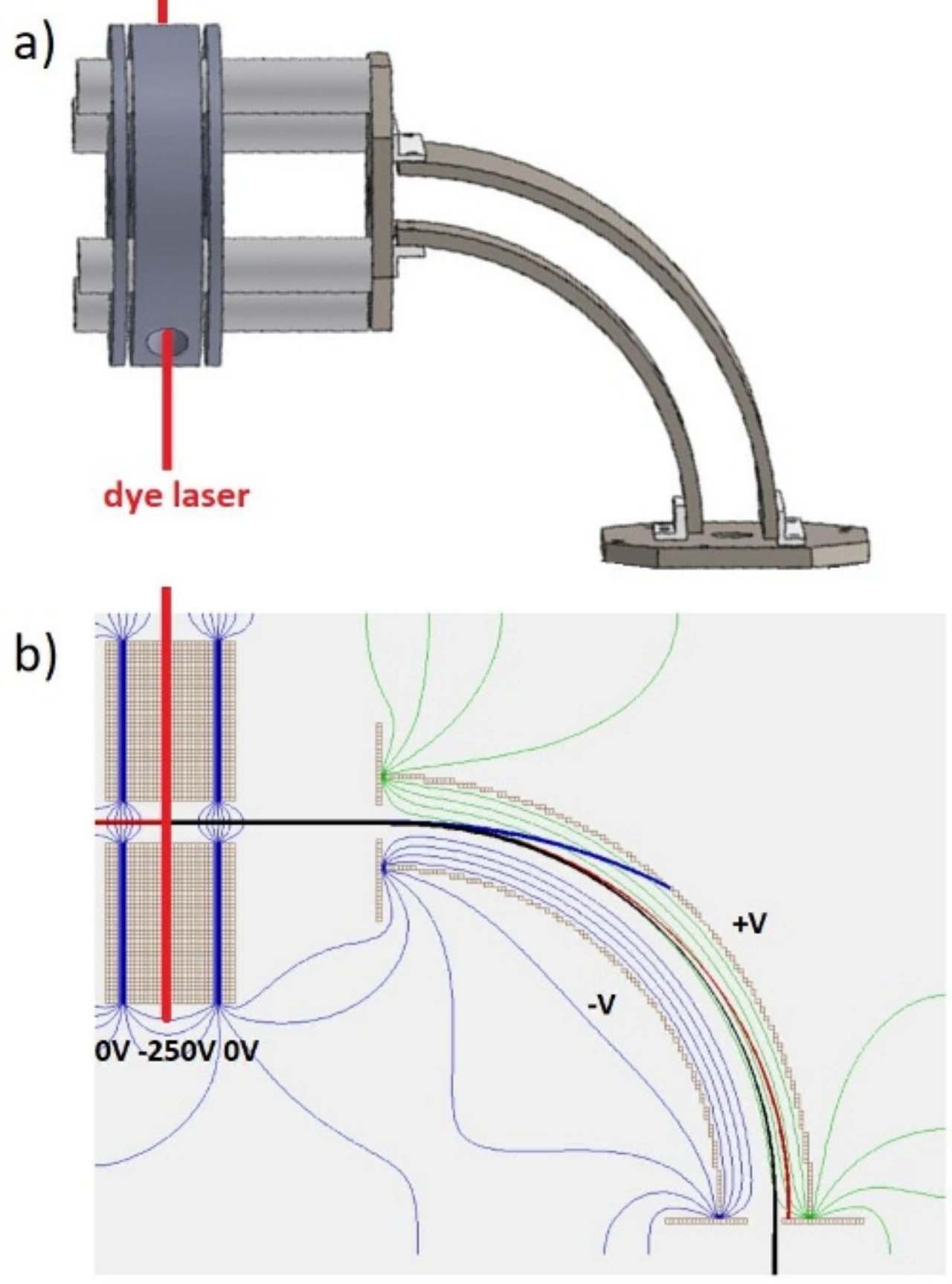
a)
dye laser
b)
+V
-V
0V -250V 0V

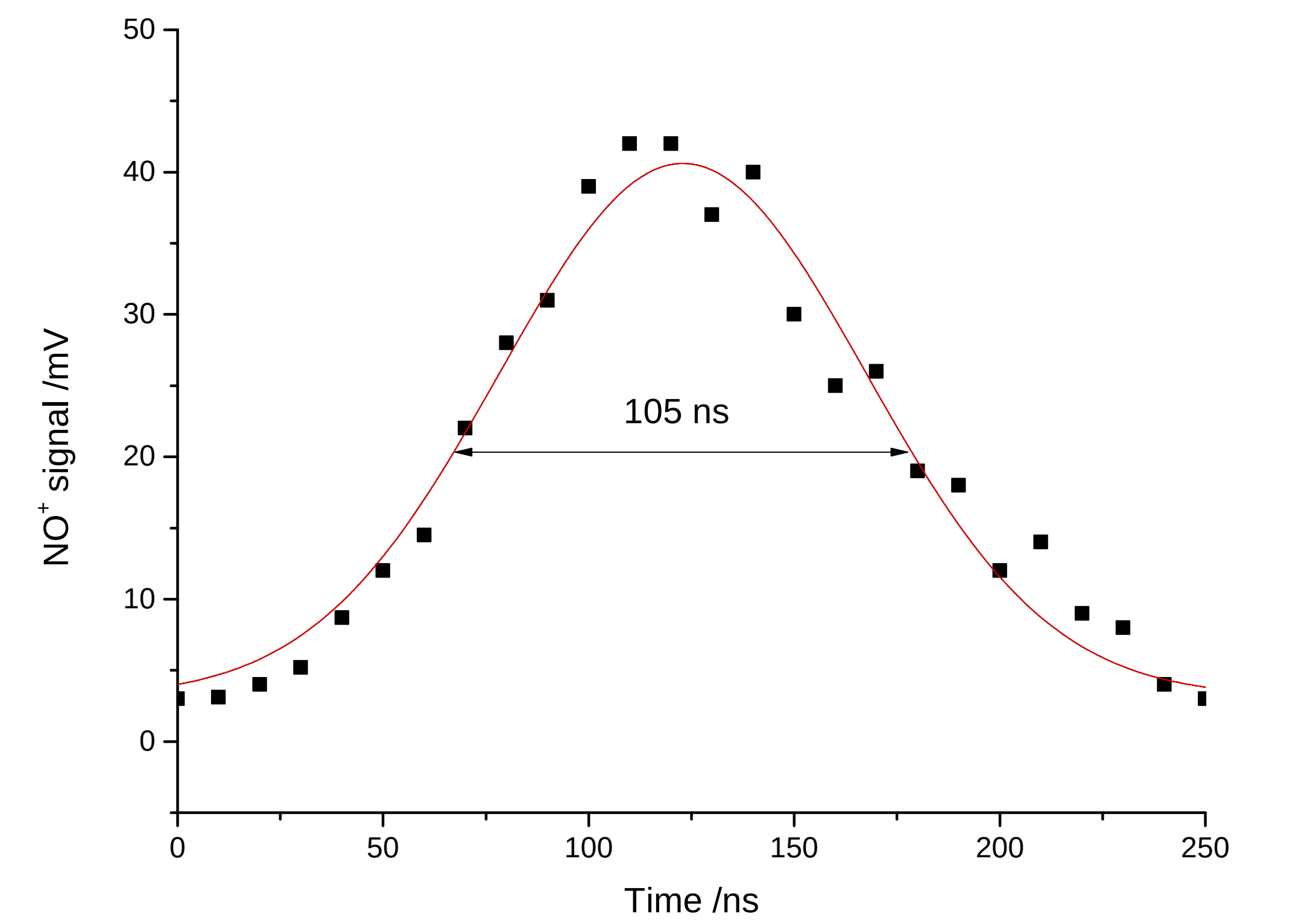
50
40
30
20
10
0
NO+ signal /mV
105 ns
0
50
100
150
200
250
Time /ns

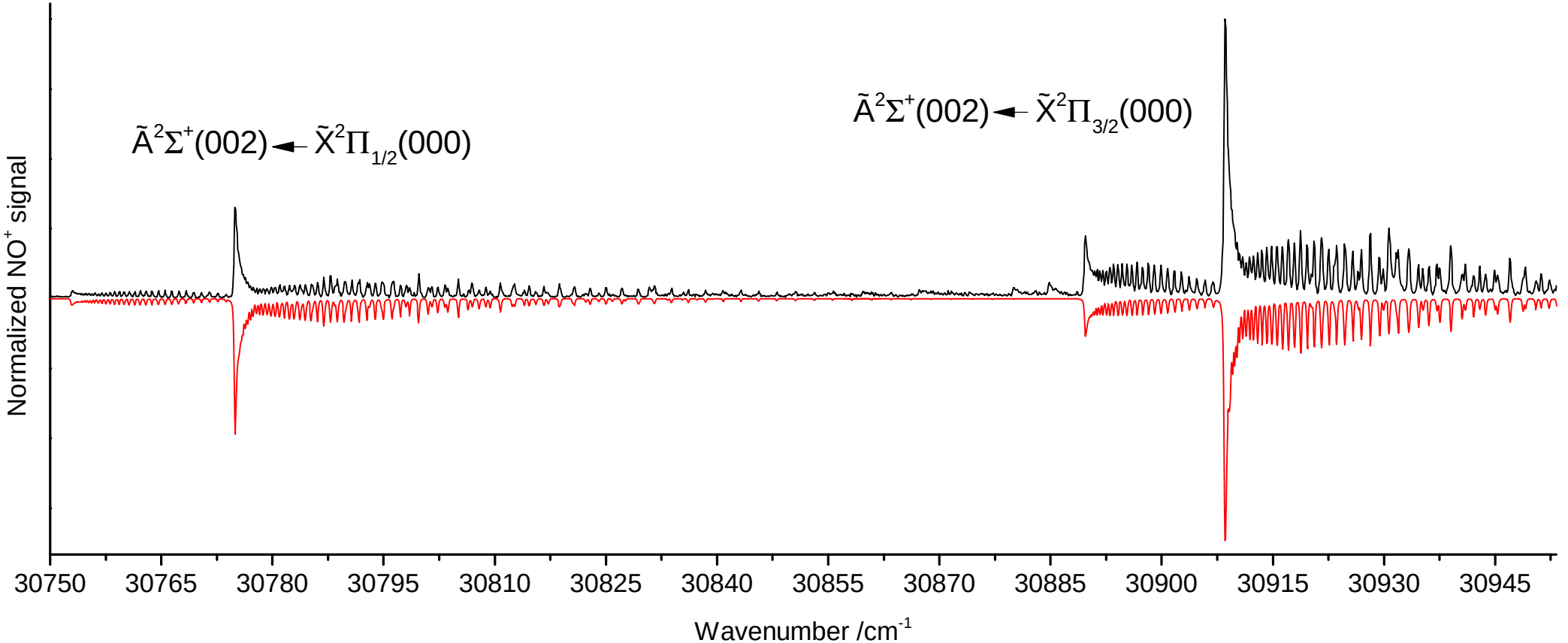
$\tilde{A}^2\Sigma^+(002) \leftarrow \tilde{X}^2\Pi_{1/2}(000)$
$\tilde{A}^2\Sigma^+(002) \leftarrow \tilde{X}^2\Pi_{3/2}(000)$
Normalized NO^+ signal
30750
30765
30780
30795
30810
30825
30840
30855
30870
30885
30900
30915
30930
30945
Wavenumber /cm^{-1}

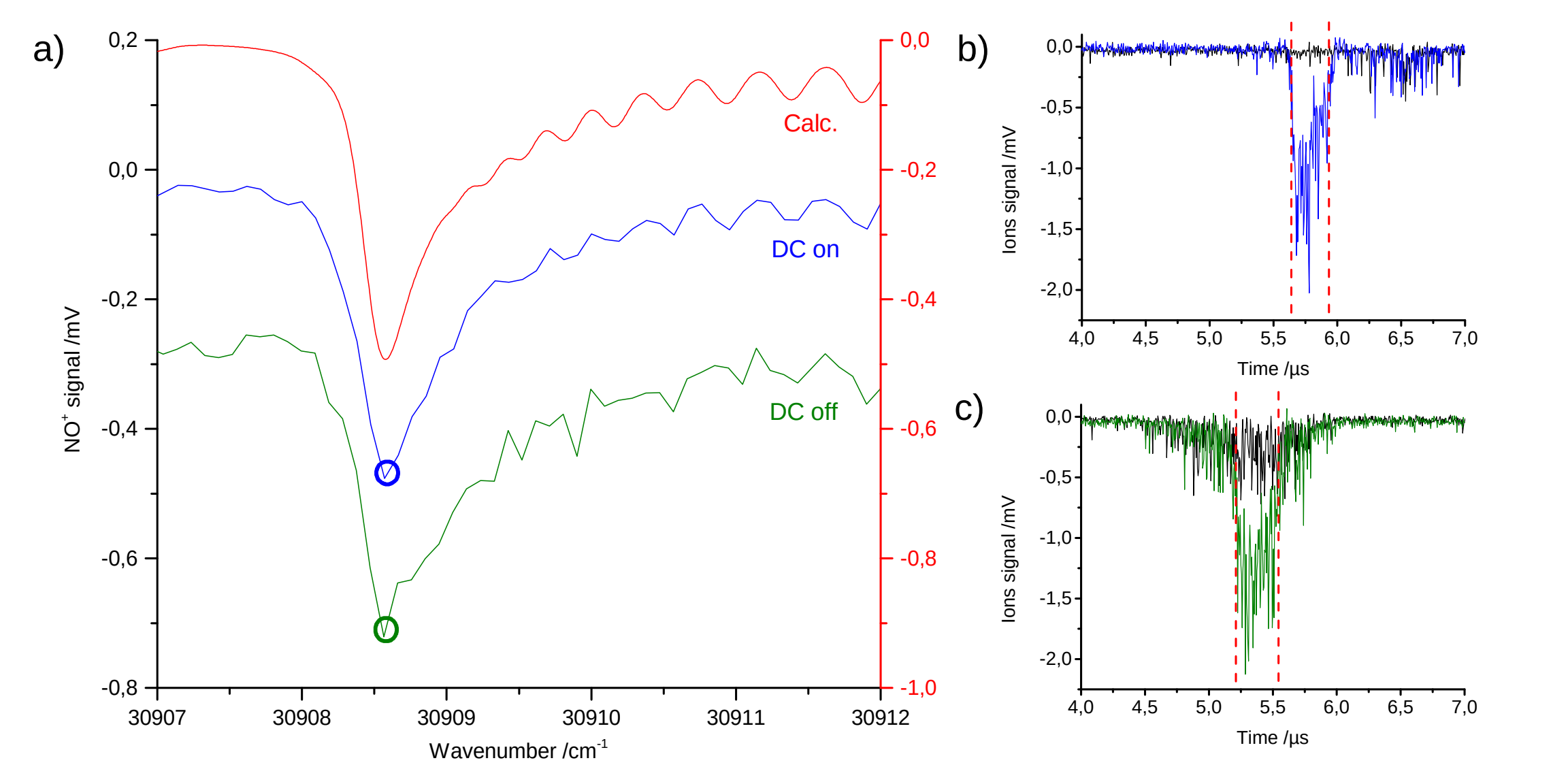
a)
b)
c)
Calc.
DC on
DC off
NO+ signal /mV
Wavenumber /cm-1
Ions signal /mV
Time /µs
0,2
0,0
-0,2
-0,4
-0,6
-0,8
-1,0
-1,5
-2,0
30907
30908
30909
30910
30911
30912
4,0
4,5
5,0
5,5
6,0
6,5
7,0

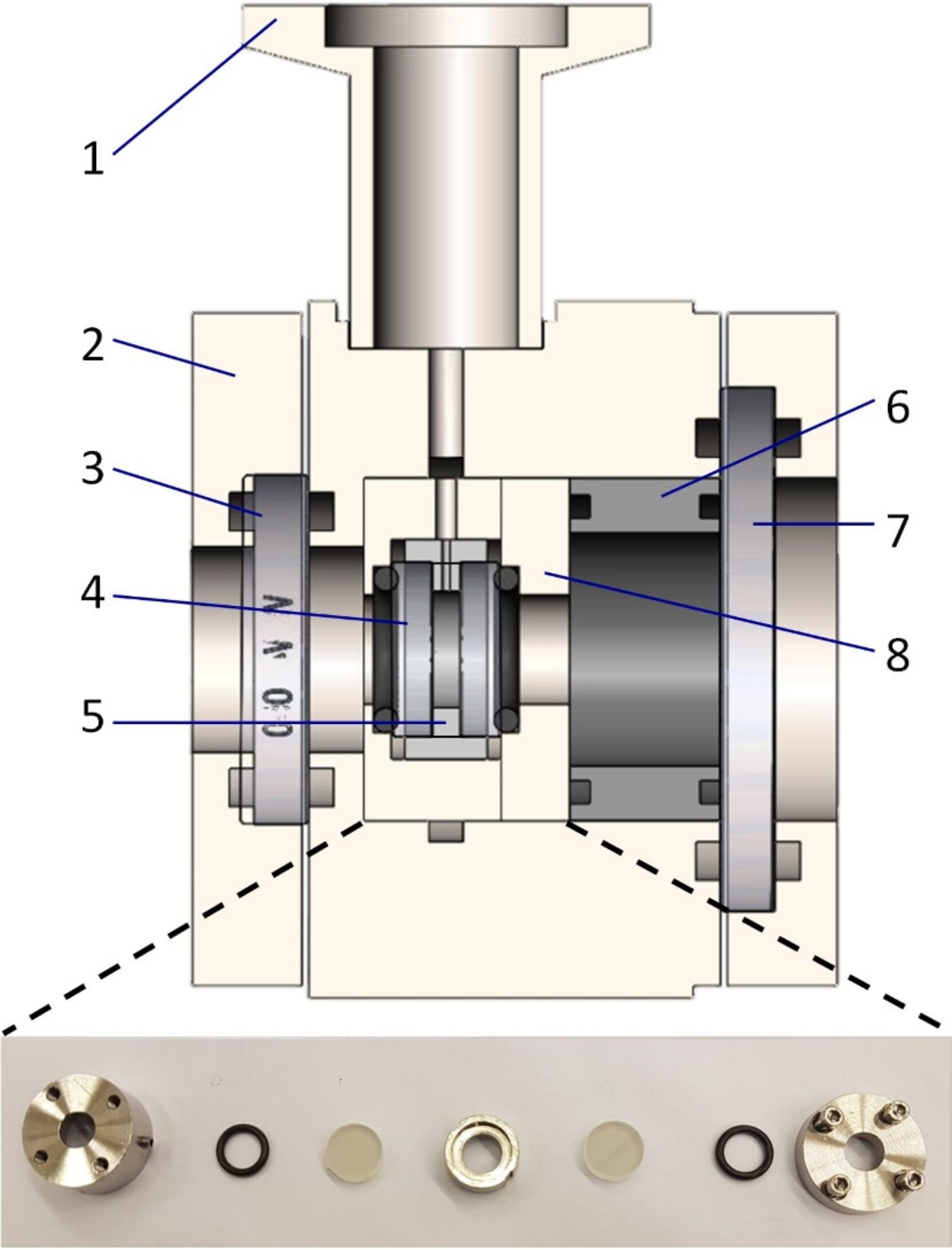
1
2
3
4
5
6
7
8

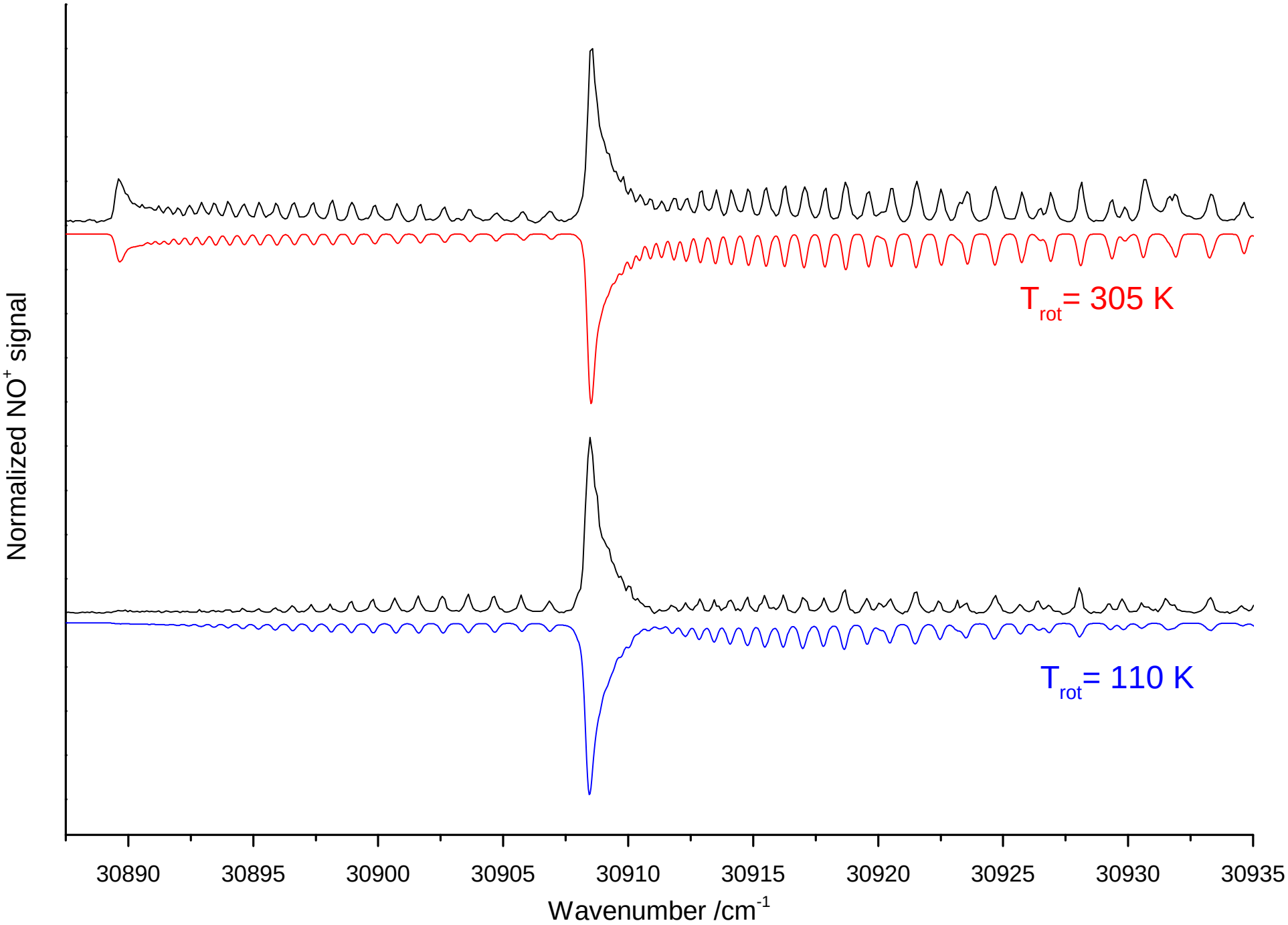
Normalized NO+ signal
T rot = 305 K
T rot = 110 K
30890
30895
30900
30905
30910
30915
30920
30925
30930
30935
Wavenumber /cm-1

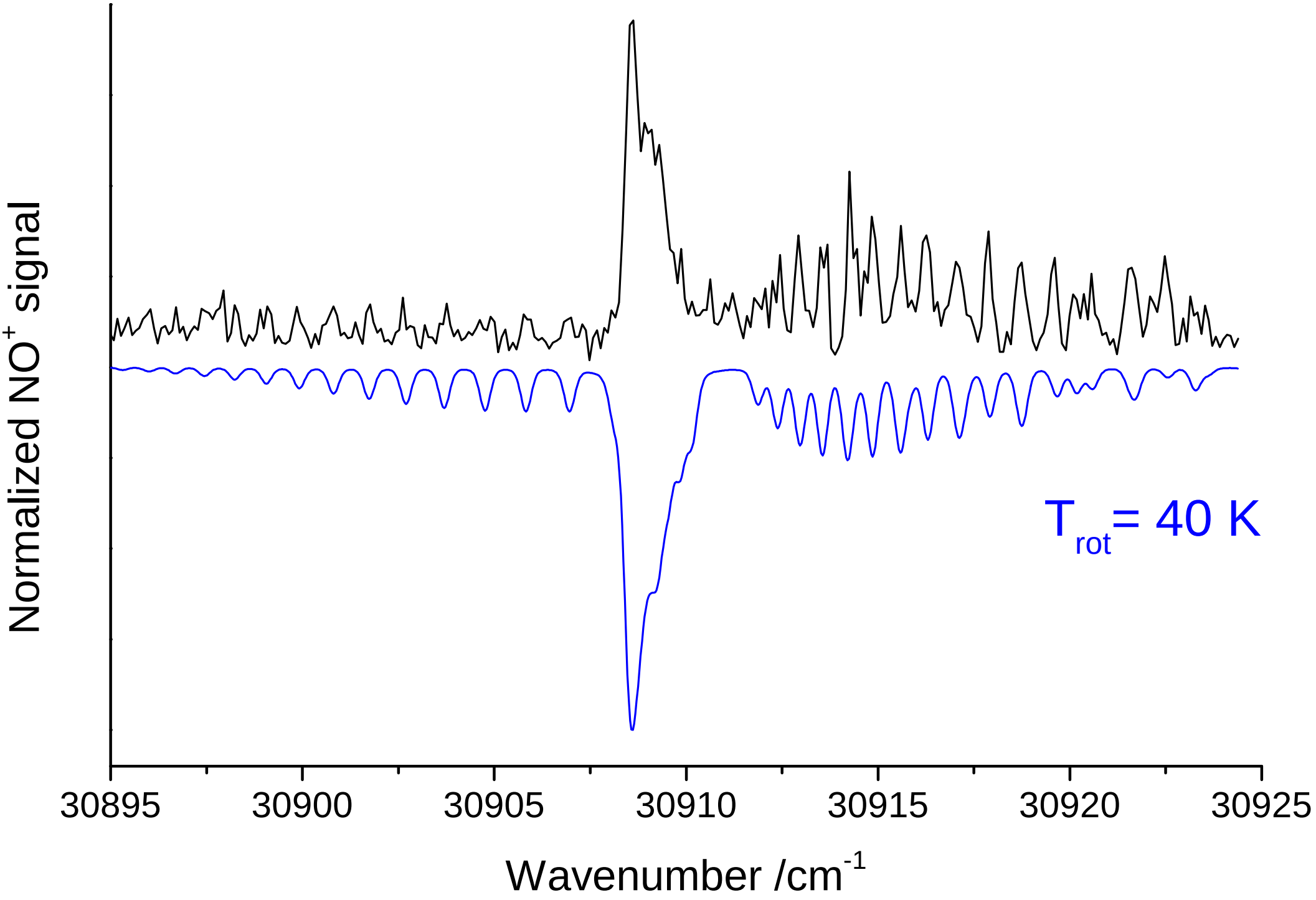
Normalized NO+ signal
30895
30900
30905
30910
30915
30920
30925
Wavenumber /cm-1
Trot= 40 K